INSTITUTE OF PHYSICS PUBLISHING REPORTS ON PROGRESS IN PHYSICS

Rep. Prog. Phys. **64** (2001) 1759–1814 PII: S0034-4885(01)82269-7

Magnetoencephalography—a noninvasive brain imaging method with 1 ms time resolution

Cosimo Del Gratta[1,2,3], **Vittorio Pizzella**[1,2,3], **Franca Tecchio**[4] **and Gian Luca Romani**[1,2,3]

[1] Department of Clinical Sciences and Bioimaging, University 'G D'Annunzio', Chieti, Italy
[2] ITAB—Institute for Advanced Biomedical Technologies, University 'G D'Annunzio', Chieti, Italy
[3] INFM—National Institute for the Physics of Matter, Research Unit of L'Aquila, Italy
[4] IESS—Institute for Solid State Electronics, National Council of Research, Rome, Italy

Received 26 June 2001, in final form 6 September 2001
Published 15 November 2001
Online at stacks.iop.org/RoPP/64/1759

Abstract

The basics of magnetoencephalography (MEG), i.e. the measurement and the analysis of the tiny magnetic fields generated outside the scalp by the working human brain, are reviewed. Three main topics are discussed: (1) the relationship between the magnetic field and its generators, including on one hand the neurophysiological basis and the physical theory of magnetic field generation, and on the other hand the techniques for the estimation of the sources from the magnetic field measurements; (2) the instrumental techniques and the laboratory practice of neuromagnetic field measurement and (3) the main applications of MEG in basic neurophysiology as well as in clinical neurology.

(Some figures in this article are in colour only in the electronic version)

Contents

	Page
1. Introduction and historical background	1761
2. Generation of neuromagnetic fields: neurophysiological basis	1761
2.1. A common difficulty in bioelectromagnetic studies: the inverse and forward problem	1761
2.2. The neuron: membrane ionic exchanges	1762
2.3. Action potentials and postsynaptic potentials	1764
2.4. Current pattern produced by neural excitations	1765
3. Generation of neuromagnetic fields: physical theory	1767
3.1. The quasi-static approximation of Maxwell's equations	1767
3.2. Magnetic field and electric potential in an infinite homogeneous medium	1769
3.3. Magnetic field and electric potential for a piecewise homogeneous medium	1771
4. The forward problem: modelling of source and volume conductor	1773
4.1. Source modelling	1773
4.2. The spherical volume conductor model	1776
4.3. A realistic volume conductor model: the boundary element method (BEM)	1777
5. The inverse problem: reconstruction of neural sources	1780
5.1. Single-current-dipole solutions	1781
5.2. Multiple-current-dipole solutions	1782
5.3. Linear estimation	1784
5.4. Lead field theory	1785
6. Instrumentation for magnetoencephalography	1786
6.1. The SQUID	1787
6.2. The single-channel biomagnetic system	1788
6.3. Magnetic noise rejection	1792
6.4. Multichannel neuromagnetic systems	1794
7. Data acquisition and analysis	1794
7.1. Analogue signal processing	1795
7.2. Analogue-to-digital conversion	1795
7.3. Digital signal processing and data acquisition	1796
7.4. Data analysis	1797
8. Applications of magnetoencephalography in basic research	1798
8.1. Spontaneous brain activity	1798
8.2. Evoked activity	1800
8.3. Cognitive functions	1802
8.4. Physiological plasticity	1804
9. Clinical applications of magnetoencephalography	1804
9.1. Pre-surgical mapping: visual, auditory, somatosensory and motor cortex characterization	1804
9.2. Identification of epileptogenic areas: single interictal spikes and seizure generator identification	1804
9.3. Plasticity following central and peripheral lesions	1805

9.4. Psychiatric studies 1806
9.5. Neurological dysfunction studies 1806
10. Conclusion 1807
References 1809

1. Introduction and historical background

The first attempt at detecting a magnetic signal originating from the human brain can be traced back to the late 1960s, and was performed by means of a nonsuperconducting sensor (Cohen 1968). Two years later a superconducting quantum interference device (SQUID) was used for the first time to reveal a biomagnetic signal, originating from the human heart (Cohen *et al* 1970), and only after two more years was the same instrument used successfully to record a human magnetic alpha rhythm with a satisfactory signal-to-noise ratio (Cohen 1972). A few years later (Brenner *et al* 1975), magnetic signals associated with brain activity evoked by peripheral sensory stimulation were also detected.

The first demonstration of the novel and original capability of the neuromagnetic method, i.e. the possibility of three-dimensionally localizing sources of cerebral activity, was due to the fortunate combination of two studies performed at the beginning of the 1980s: the theoretical analysis of the properties of magnetic signals originating from bioelectric currents and their relationship to the surrounding medium (Williamson and Kaufman 1990), and the intuition that that analysis could be applied to interpret real data, in the form of field maps, to investigate the properties of the human auditory cortex. Romani and co-workers (1982) demonstrated that the organization of the primary auditory cortex indeed follows a logarithmic structure, with sounds of increasing frequency projected in progressively deeper sites of the cortex and, at the same time, that the brain devotes an equal number of neurons to each octave of sound. Another significant step forward was taken in the same period, with the identification of the first clinical application of the neuromagnetic method, namely the study of focal epilepsy (Modena *et al* 1982, Barth *et al* 1982, 1984, Chapman *et al* 1983). From an instrumental point of view, it should be stressed that all these studies were performed using single SQUIDs, namely single-channel instruments. The technological content of a SQUID-based biomagnetic system will be clear in the following, as well as the difficulties that—in the successive 15 years—characterized the relative slowness in developing larger and larger systems. Actually, it was only in the second half of the 1990s that systems able to simultaneously map magnetic fields over the whole scalp, namely whole-head systems, became available. With the help of these systems, it is now possible to perform sophisticated studies on basic functions of the brain, exploring both the primary and secondary sensory areas, and the cognitive functions, such as those associated with memory, attention, language etc. Additionally, the availability of large systems has raised the interest of clinicians and today magnetoencephalography (MEG) is used routinely in numerous hospital laboratories as a methodology complementary to PET and fMRI to investigate brain diseases such as epilepsy, Parkinson's disease, Alzheimer's disease and stroke and, last but not least, to perform presurgical mapping.

The aim of this paper is to present a review of the state of the art of the instrumentation used in neuromagnetic measurement as well as of the mathematical modelling that underlies the interpretation of the experimental data. Finally the most significant results achieved in basic research and in the clinical application of the method will be illustrated, without pretending to be exhaustive but with the aim of providing a hint of what is nowadays possible with what we can undoubtedly consider the most successful application of superconducting magnetometers.

2. Generation of neuromagnetic fields: neurophysiological basis

2.1. A common difficulty in bioelectromagnetic studies: the inverse and forward problem

The identification of a specific electrical source configuration from a measured distribution of electric potentials and/or magnetic fields—namely the *inverse* problem—represents one of

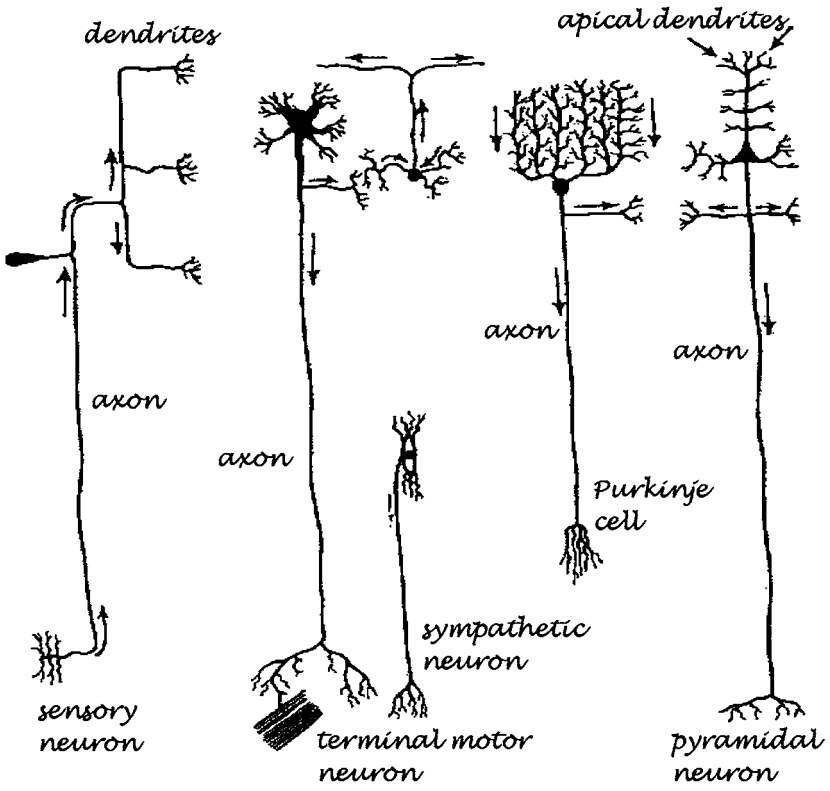

Figure 1. Different types of neuron as encountered in the human brain.

the most challenging aspects investigators face when trying to interpret biomagnetic signals. Indeed, the inverse problem has no unique solution, since an infinite number of source configurations can account for the measured field distribution. The introduction of some constraint, such as a specific mathematical model to be used as the signal source, permits one to solve the problem and achieve source identification. This procedure will be described in detail later on: in order to understand the motivations that suggest the use of a specific model rather than some other one, it is necessary to describe in some detail the mechanisms underlying the physiology of neural cells, the ionic exchanges at the level of the cell membrane, the origin of action potentials and their propagation along the nervous system, and the synaptic connection as well as the generation of postsynaptic potentials.

2.2. The neuron: membrane ionic exchanges

The basic constituent of the central nervous system is the *neuron*: it belongs to the class of so-called *excitable cells*, i.e. cells that in their resting state are characterized by a voltage difference between the inside and the outside of a membrane that completely surrounds the cell itself and features a selective permeability to specific ion populations. Neurons have different shapes, as shown in figure 1, but all consist of (1) a cellular body, containing the nucleus and the cytoplasm, (2) several dendrites, small and short branches that usually connect the neurons with adjacent ones and (3) an axon, an extended protruding filament, that can be as long as one metre, and permits propagation of electric signals, i.e. information, along tracts within the

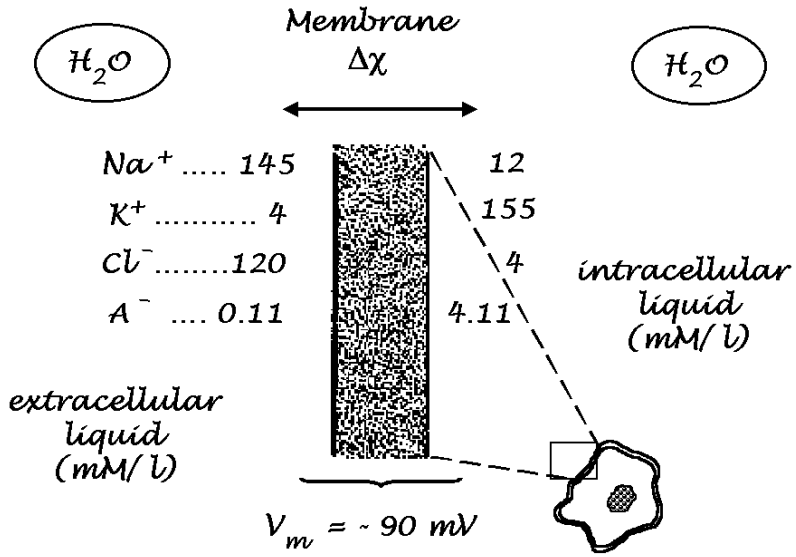

Figure 2. Distribution of different ion populations across the membrane.

nervous system. All these portions of the neuron are contained within the neural membrane that therefore separates the cytoplasm from the extra-cellular fluid.

Ionic currents in the cerebral cells produce magnetic fields. This phenomenon arises from general physical behaviour predicted by Ampère's law and summarized by the Biot–Savart law: whenever an electric current flows, a magnetic vector field is generated in the surrounding space. This statement is valid for any conductor along which a current flows, and holds also for neural cells, where the role of 'moving electric charges' is basically played by Na^+ and K^+ ions. Indeed there are other ionic populations more or less participating in the membrane polarization—such as Cl^- ions and large negative anions (A^-)—but the basic mechanism of depolarization and repolarization of the neural membrane can be essentially explained by taking into account displacement of Na^+ and K^+ ions. The cell membrane consists of a double layer of phospholipids spanned by proteins. The hydrophilic head groups of the phospholipids are in contact with the water in the intracellular medium on one side and with the extracellular medium on the other side, whereas the hydrophobic tails of one layer are in contact with those of the other layer in the middle of the membrane. This configuration gives the membrane a high electrical resistance: for example, the membrane of a 1 mm long segment of a 100 μm diameter nerve axon has a resistance of 300 kΩ (Wikswo 1989). The proteins have an axial channel that allows certain ions to cross the cell membrane, thus making the membrane selectively permeable to several ion species. Some of the proteins are gated, i.e. voltage dependent, which means that these proteins allow passage of ions only when they are in a specific configuration, depending on the transmembrane potential.

The neural membrane separates the inside of the neuron from the external medium. In normal conditions, namely the equilibrium state, there is a different concentration of ionic populations inside and outside the cell: in particular, K^+ ions are much more abundant inside the membrane than outside, whereas Na^+ ions feature an opposite concentration gradient.

Figure 2 illustrates schematically the distribution of different ion populations across the membrane. The equilibrium condition is therefore based on a strong concentration gradient that is maintained only because of the selective permeability of the membrane.

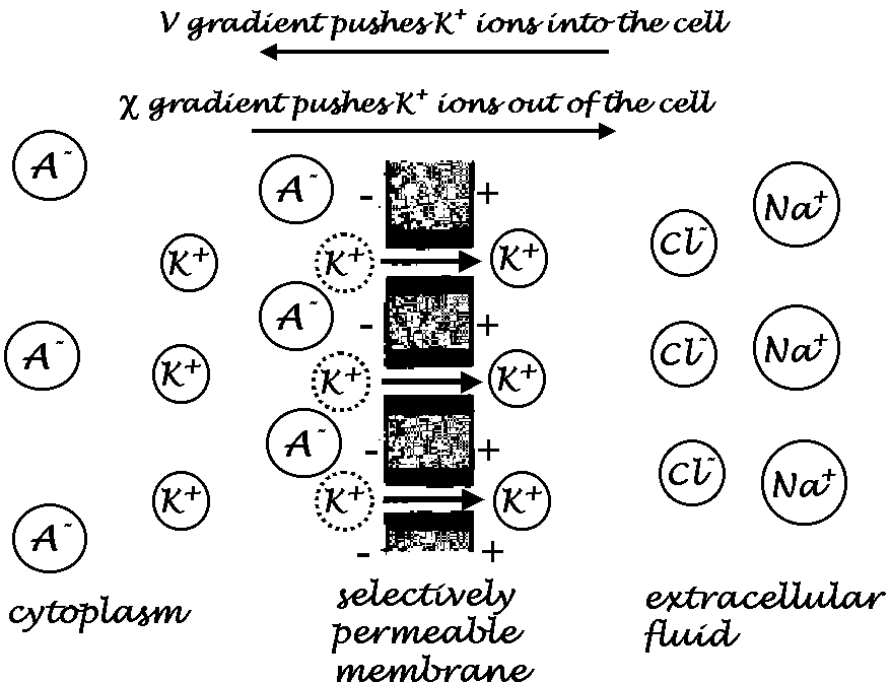

Figure 3. Membrane and ionic distribution at the equilibrium state.

The Nernst equation permits calculation of the voltage difference across the neuron membrane due to the concentration difference for each ionic species: the resulting transmembrane *resting potential* is about −90 mV. The equilibrium concentration gradient $\Delta\chi$ is therefore associated with an equilibrium potential gradient: this situation—schematically depicted in figure 3—is maintained as long as the selective permeability of the membrane gates does not change and thanks to an active device, the so-called Na/K *pump*, continuously provides an exchange of Na^+ versus K^+ ions across the membrane. Each cycle of the pump expels three Na^+ ions out of the cell and introduces two K^+ ions into the cell. The concentration gradient is maintained by the action of the Na–K pump, which uses metabolic energy derived from ATP.

2.3. Action potentials and postsynaptic potentials

If a perturbation to the resting potential occurs, for instance due to interference from another neuron, of from an external stimulation, and if the perturbation is larger than a threshold value, then the Na^+ gates open coherently: as a consequence of the strong concentration gradient, a sudden inflow of Na^+ ions occurs, producing a simultaneous increase of the potential difference across the membrane, from −70 to about +20 mV. When this potential level is reached, the Na^+ gates close and the K^+ gates open in turn. The strong gradient again pushes K^+ ions out of the intracellular space, at a slightly lower speed than the previous inflow, and this outflow continues until a potential difference equal to the resting potential is achieved. The complete phenomenon—illustrated schematically in figure 4, that includes a depolarization of the membrane and its successive repolarization, lasts less than 3 ms. The equilibrium condition is restored but the Na^+ versus K^+ ionic concentration is inverted with respect to the initial state:

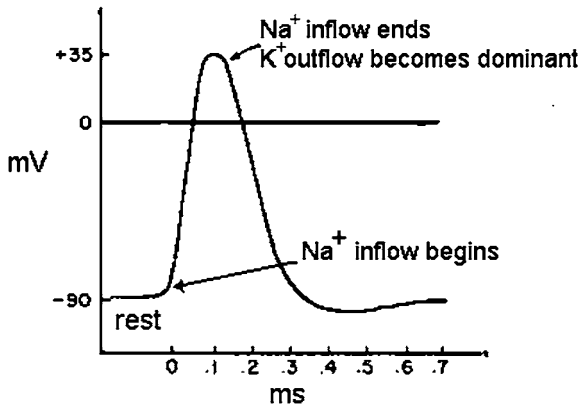

Figure 4. Schematic pattern of the voltage variation associated with an action potential.

the appropriate respective abundance of Na^+ and K^+ ions will be re-established in a longer time period, during which the membrane cannot undergo a new depolarization, by the action of the Na/K pump (Koester 1985).

The phenomenon described above is referred to as an *action potential*, and has the particular feature of being self-propagating: indeed the sudden depolarization and repolarization of the membrane in a specific site acts as a new perturbation for the adjacent portion of the membrane itself. The excitation therefore propagates along the neuron at a high speed: in peripheral neurons a speed as high as 50 m s^{-1} can be achieved. It should be stressed for the purposes of this section that the overall excitation, i.e. the action potential, consists of a rapid depolarization front followed by an almost equally fast repolarization front. Both the axon and the dendrites terminate in a *synapse* that allows signal transmission from one cell to another by chemical means, namely the *neurotransmitters*. The propagation of the excitation is therefore mediated by the synapse, and occurs at a much longer timescale. The voltage variations associated with synaptic transmission are called *postsynaptic potentials*. They consist of a slow depolarization wave followed by a much slower repolarization. In comparison with the action potential, the postsynaptic potential may last several tens or hundreds of milliseconds (Williamson and Kaufmann 1990).

2.4. Current pattern produced by neural excitations

We want to dwell a little on the current patterns associated with the two main events described above, the action potential and the postsynaptic potentials, since they have a fundamental importance for the structure of the generated magnetic fields. Figure 5(*a*) schematically depicts the pattern of ionic currents which flow inside, across and outside the membrane of a neuron, and specifically in a portion of it, such as an axon or a dendritic tree, in correspondence with a depolarization front.

The first point we want to make is in regard to the distribution of ionic currents: the *intracellular current* is basically a concentrated ionic flow inside the membrane, and along it in a very small portion of the total dendritic or axonal length. This is represented by an arrow in figure 5(*a*), and is what is accounted for by the simplest and most used model source, namely a *current dipole* (see section 4). The *transmembrane current* follows a radial pattern, in that it flows isotropically through a cross section of the 'cylindrically' shaped neural membrane. The *extracellular current* flows backward in the surrounding medium in order to close the loop and

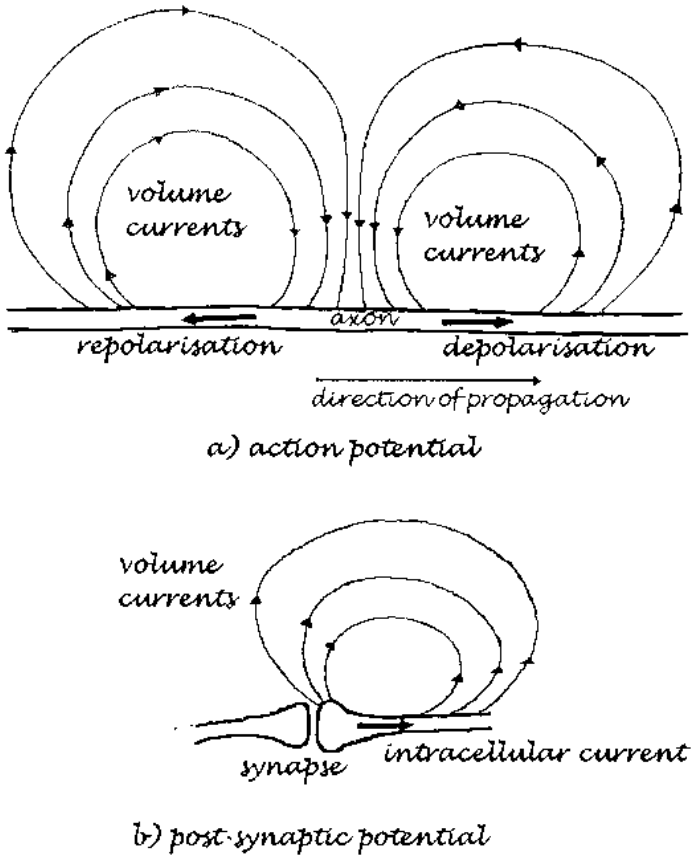

Figure 5. Schematic current pattern associated with (*a*) an action potential and (*b*) a postsynaptic potential.

satisfy the current continuity requirement. Differently from what happens to the intracellular current, the pattern is now widespread in the surrounding medium, but again an axial symmetry is maintained, at least as far as the medium has homogeneous conductivity.

The second point concerns the time evolution of this bioelectric event. As said, the pattern illustrated in figure 4 actually represents a *depolarization* process, with respect to the 'unperturbed' resting state of the membrane. This phenomenon is followed by a *repolarization* process, during which the transmembrane potential returns to its initial state. In this second event the overall current pattern is reversed, with the intracellular current pointing backward and the extracellular current pointing in a forward direction. Both the depolarization and repolarization *fronts* move rapidly along the axon as a propagating excitation, and are linked together and separated by less than a few milliseconds in time, and less than a few millimetres in space.

By contrast, the current pattern associated with postsynaptic potentials (figure 5(*b*)) is basically that originating from the much slower repolarization process. It is relatively localized at a cortical level and may usually involve several thousands of adjacent dendrites.

The substantial difference in the timescale supports the idea that action potential currents, beside their evident role in the peripheral nervous system, are also responsible for measured brain-stem activity and, possibly, for very early components of cortical response. On the other

hand, postsynaptic currents, such as those involving apical dendrites of pyramidal neurons which feature a preferential alignment perpendicularly to the cortical surface, are commonly believed to generate stimulus- and event-related responses.

3. Generation of neuromagnetic fields: physical theory

In the previous section, some aspects of brain cellular and functional organization that are relevant to MEG were reviewed. In this section, we shall outline the bioelectromagnetic field theory that is relevant to the modelling of neuromagnetic data. The topics of this section are the statement of the assumptions that simplify Maxwell's equations in the description of the neuromagnetic field, the relationship between field and currents in an infinite homogeneous conducting space and a general expression for the neuromagnetic field that allows us to take into account the gross inhomogeneities of the head. The latter expression will be the basis for the modelling of neuromagnetic data in the next section. The subject of bioelectric and biomagnetic field theory is extensively treated in the literature. For a comprehensive description, and for related topics, we suggest the books by Gulrajani (1998), Malmivuo and Plonsey (1995), and Titomir and Kneppo (1994).

3.1. The quasi-static approximation of Maxwell's equations

In this section we wish to clarify the assumptions adopted to simplify Maxwell's equations, based on the physical properties of the head as a conductor, and of the currents flowing in it as a result of neural activity. The general theoretical context in which neuromagnetic phenomena are described is that of electromagnetic theory of continuous macroscopic media. Maxwell's equations for polarizable and magnetizable media are given by

$$\text{curl}\, \boldsymbol{E} = -\partial \boldsymbol{B}/\partial t \tag{3.1}$$

$$\text{curl}\, \boldsymbol{H} = \boldsymbol{J} + \partial \boldsymbol{D}/\partial t \tag{3.2}$$

$$\text{div}\, \boldsymbol{D} = \rho \tag{3.3}$$

$$\text{div}\, \boldsymbol{B} = 0 \tag{3.4}$$

where $\boldsymbol{E}$ and $\boldsymbol{H}$ are the electric and magnetic field respectively, $\boldsymbol{D}$ and $\boldsymbol{B}$ are the electric displacement and the magnetic induction respectively and ρ and $\boldsymbol{J}$ are the electric charge and electric current density respectively.

From equations (3.2) and (3.3) follows the law of conservation of charge:

$$\text{div}\, \boldsymbol{J} + \partial\rho/\partial t = 0. \tag{3.5}$$

To the above equations we must add the constitutive relations that describe the macroscopic electric and magnetic properties of the media. As will be seen in the following, the bioelectric and biomagnetic fields are weak enough to justify the assumption that the constitutive relations are linear:

$$\boldsymbol{D} = \varepsilon \boldsymbol{E} \tag{3.6}$$

$$\boldsymbol{B} = \mu \boldsymbol{H}. \tag{3.7}$$

We shall further assume that the tissue is isotropic, so that the electric permittivity ε and magnetic permeability μ are represented by scalars. In the more general linear case, these quantities are represented by symmetric tensors of rank two. The magnetic permeability may be practically considered to be equal to the magnetic permeability of vacuum, since most living tissue is only weakly diamagnetic, with a magnetic susceptibility close to that of water ($\chi = -9 \times 10^{-6}$), so that $\mu = (1 + \chi)\mu_0 \approx \mu_0$.

We are interested here in the electric potential and the magnetic field generated by bioelectric currents flowing inside the head. The latter are represented by the current source density $\boldsymbol{J}$ of equations (3.2) and (3.5) which is defined in some region of space—called the *volume conductor*—where an electric conductivity function σ is also defined. Here, again, σ will be considered to be a scalar function, implying that the conductivity is isotropic. We consider that the currents consist, on one hand, of active ion displacements related directly to electrochemical cell activity—such as ions crossing the cell membrane or flowing in a dendrite, and, on the other hand, of the passive displacement of free ions under the action of the electric field generated in the surrounding tissue by cell activity. The former are usually termed *impressed* currents, while the latter are called *volume* currents. Therefore the current density at any point in the conductor will be expressed as the sum of two terms:

$$\boldsymbol{J} = \boldsymbol{J}^i + \boldsymbol{J}^v \tag{3.8}$$

where the superscripts stand for the impressed and volume current density respectively. From the generalized form of Ohm's law:

$$\boldsymbol{J}^v = \sigma \boldsymbol{E}. \tag{3.9}$$

We obtain

$$\boldsymbol{J} = \boldsymbol{J}^i + \sigma \boldsymbol{E}. \tag{3.10}$$

Let us now examine equation (3.2), taking (3.10) into account:

$$\operatorname{curl} \boldsymbol{H} = \boldsymbol{J}^i + \sigma \boldsymbol{E} + \partial \boldsymbol{D}/\partial t. \tag{3.11}$$

We shall now show that the intensity of the displacement current density is negligible compared with the volume current density in the usual range of frequencies of neuromagnetic fields, extending from dc to about 10^3 Hz, when we include signals due to action potentials such as those propagating in the brain stem or in the peripheral nervous system. Let us consider a sinusoidal component of the impressed current density at frequency f. Then the electric field in the volume conductor will also be sinusoidal. The second and third terms on the right-hand side of (3.11) may be expressed as

$$\sigma \boldsymbol{E} = \sigma \boldsymbol{E}_0 \sin(2\pi f t) \tag{3.12}$$

$$\partial \boldsymbol{D}/\partial t = 2\pi f \varepsilon \boldsymbol{E}_0 \cos(2\pi f t). \tag{3.13}$$

The displacement current term may therefore be neglected if $f \ll \sigma/(2\pi\varepsilon)$. This condition is satisfied for frequencies lower than a few thousand hertz. To estimate a lower bound for the quantity $\sigma/(2\pi\varepsilon)$, we may consider limiting values for σ and ε. For brain tissue, $\sigma > 10^{-1}\ \Omega^{-1}\ \mathrm{m}^{-1}$, and $\varepsilon \leqslant 5 \times 10^4 \varepsilon_0$, yielding $\sigma/(2\pi\varepsilon) \geqslant 36\,000$ Hz.

Then, we shall show that Faraday induction in equation (3.1) contributes negligibly to the electric field at the usual frequencies of neuromagnetic phenomena. Let us consider the integral form of this equation and use it to calculate the circulation, around a circular path of radius R, of the electric field E induced by a uniform oscillating magnetic field $B = B_0 \sin(2\pi f t)$ inside the head. From this circulation, the intensity of the induced electric field may be obtained:

$$E = \pi R f B_0 \cos(2\pi f t). \tag{3.14}$$

Typical intensities of the neuromagnetic field, measured outside the head, range from 10^{-13} T for evoked fields to 10^{-12} T for alpha activity. In the latter case, we may extrapolate a mean value for B_0 inside the head of 10^{-9} T. Taking 0.1 m for R, and 100 Hz for f, we obtain for the induced electric field $E \approx 10^{-8}\ \mathrm{V\ m}^{-1}$. On the other hand, typical potential differences measured over the scalp are about 1×10^{-6} V, from which a value of $10^{-5}\ \mathrm{V\ m}^{-1}$ may be

estimated for the corresponding electric field. As we can see, the induced electric field is three orders of magnitude smaller than the latter figure and can therefore be neglected.

The above considerations show that the terms with time derivatives contribute negligibly to the fields. However, these terms do not act only as sources of the fields, since their presence in Maxwell's equations implies a dephasing of the fields with respect to the sources due to capacitance in the tissues, or to finite signal propagation velocity, as well as a reduced intensity of the fields in the case of capacitive impedance, with respect to pure resistance. All these effects have been shown to be negligible in the case of bioelectric and biomagnetic fields on the basis of the estimated tissue conductivity and electric permittivity values. A detailed discussion of this topic would be too long to present here, but may be found in the work of Gulrajani (1998) p 192 and Titomir and Kneppo (1994) p 13.

In conclusion, we may neglect in Maxwell's equations the terms corresponding to the displacement current and to Faraday induction. We are then left with the quasi-static Maxwell equations, that may be taken as the basis for a description of biomagnetic phenomena.

$$\text{curl}\, \boldsymbol{E} = 0 \tag{3.15}$$

$$\text{curl}\, \boldsymbol{B} = \mu_0 \boldsymbol{J} \tag{3.16}$$

$$\text{div}\, \boldsymbol{E} = \rho/\varepsilon \tag{3.17}$$

$$\text{div}\, \boldsymbol{B} = 0. \tag{3.18}$$

The equation for the conservation of charge becomes

$$\text{div}\, \boldsymbol{J} = 0. \tag{3.19}$$

From now on, we shall not use the vectors $\boldsymbol{H}$ and $\boldsymbol{D}$, and the vector $\boldsymbol{B}$ will be referred to simply as the magnetic field.

3.2. Magnetic field and electric potential in an infinite homogeneous medium

We shall now derive some basic properties of the electric potential and the magnetic field generated by bioelectric currents. We shall for the moment restrict the derivation to the simple case of an infinite homogeneous medium. This means that the volume conductor extends to infinity and its conductivity is uniform. Substituting (3.10) into (3.19) we obtain

$$\text{div}\, \boldsymbol{E} = -\text{div}\, \boldsymbol{J}^i/\sigma. \tag{3.20}$$

Due to (3.15) we may express the electric field as the negative gradient of the electric potential Φ:

$$\boldsymbol{E} = -\text{grad}\, \Phi. \tag{3.21}$$

Substituting (3.21) into (3.20), we obtain

$$\nabla^2 \Phi = \text{div}\, \boldsymbol{J}^i/\sigma \tag{3.22}$$

where ∇^2 is the Laplacian operator.

We obtain a similar equation for the magnetic field taking the curl of equation (3.16) and using equations (3.10) and (3.15):

$$\text{curl}\, (\text{curl}\, \boldsymbol{B}) = \mu_0\, \text{curl}\, \boldsymbol{J}^i. \tag{3.23}$$

Using the identity

$$\text{curl}\, (\text{curl}\, \boldsymbol{B}) = \text{grad}\, (\text{div}\, \boldsymbol{B}) - \nabla^2 \boldsymbol{B} \tag{3.24}$$

and equation (3.18), we obtain

$$\nabla^2 \boldsymbol{B} = -\mu_0\, \text{curl}\, \boldsymbol{J}^i. \tag{3.25}$$

Equations (3.22) and (3.25) are four Poisson equations for the electric potential and for the three components of the magnetic field. These equations show two properties of the electric potential and the magnetic field generated by a current density satisfying formula (3.10), in an infinite homogeneous medium. First, Φ and $\boldsymbol{B}$ depend only on the impressed current, and not on volume current. In an infinite homogeneous conductor, the total effect of volume current vanishes. Second, Φ and $\boldsymbol{B}$ depend, respectively, on the divergence and on the curl of the impressed current, and therefore convey independent information about the current density. Unfortunately, these properties are not preserved when the conducting medium is bounded, as in a realistic case. In such a case, $\boldsymbol{B}$ depends partly on volume current, and is not independent from Φ, as will be shown later.

It may be shown that, if the source $\boldsymbol{J}^i$ vanishes at infinity, solutions of equations (3.22) and (3.25) are given by the following formulae for the electric potential and for the magnetic field respectively:

$$\Phi_\infty(\boldsymbol{x}) = -\frac{1}{4\pi\sigma}\int \frac{\mathrm{div}'\boldsymbol{J}^i(\boldsymbol{x}')}{|\boldsymbol{x}-\boldsymbol{x}'|}\,\mathrm{d}v'. \tag{3.26}$$

$$\boldsymbol{B}_\infty(\boldsymbol{x}) = \frac{\mu_0}{4\pi}\int \frac{\mathrm{curl}'\boldsymbol{J}^i(\boldsymbol{x}')}{|\boldsymbol{x}-\boldsymbol{x}'|}\,\mathrm{d}v' \tag{3.27}$$

where $\boldsymbol{x}$ indicates the position vector of a point in space, and the integration is extended to a region containing the source $\boldsymbol{J}^i$. The subscript ∞ reminds us that these formulae are valid only in an infinite homogeneous conductor.

We may transform formula (3.26) using the identity[5]

$$\mathrm{div}\,(\boldsymbol{J}^i(\boldsymbol{x}')|\boldsymbol{x}-\boldsymbol{x}'|^{-1}) = |\boldsymbol{x}-\boldsymbol{x}'|^{-1}\mathrm{div}'\boldsymbol{J}^i(\boldsymbol{x}') + \boldsymbol{J}^i(\boldsymbol{x}')\cdot\mathrm{grad}'(|\boldsymbol{x}-\boldsymbol{x}'|^{-1}) \tag{3.28}$$

where $\cdot$ indicates a scalar product. Taking the volume integral of both sides of formula (3.28), using Gauss's theorem and the fact that the surface integral of $\boldsymbol{J}^i(\boldsymbol{x}')|\boldsymbol{x}-\boldsymbol{x}'|^{-1}$ vanishes at the boundary of a region containing the source because $\boldsymbol{J}^i(\boldsymbol{x}') = 0$, and noting that

$$\mathrm{grad}'(|\boldsymbol{x}-\boldsymbol{x}'|^{-1}) = |\boldsymbol{x}-\boldsymbol{x}'|^{-3}(\boldsymbol{x}-\boldsymbol{x}') \tag{3.29}$$

we find

$$\Phi_\infty(\boldsymbol{x}) = \frac{1}{4\pi\sigma}\int \boldsymbol{J}^i(\boldsymbol{x}')\cdot\frac{\boldsymbol{x}-\boldsymbol{x}'}{|\boldsymbol{x}-\boldsymbol{x}'|^3}\,\mathrm{d}v'. \tag{3.30}$$

Similarly, we may transform formula (3.27) using the identity[6]

$$\mathrm{curl}(\boldsymbol{J}^i(\boldsymbol{x}')|\boldsymbol{x}-\boldsymbol{x}'|^{-1}) = |\boldsymbol{x}-\boldsymbol{x}'|^{-1}\mathrm{curl}'\boldsymbol{J}^i(\boldsymbol{x}') - \boldsymbol{J}^i(\boldsymbol{x}')\times\mathrm{grad}'(|\boldsymbol{x}-\boldsymbol{x}'|^{-1}) \tag{3.31}$$

where $\times$ indicates a vector product. Taking the volume integral of both sides of formula (3.31), using Stokes theorem, the fact that the surface integral of $\boldsymbol{n}\times\boldsymbol{J}^i(\boldsymbol{x}')|\boldsymbol{x}-\boldsymbol{x}'|^{-1}$, where $\boldsymbol{n}$ is a unit vector normal to the surface, vanishes at the boundary of a region containing the source because $\boldsymbol{J}^i(\boldsymbol{x}') = 0$, and (3.29) we find

$$\boldsymbol{B}_\infty(\boldsymbol{x}) = \frac{\mu_0}{4\pi}\int \boldsymbol{J}^i(\boldsymbol{x}')\times\frac{\boldsymbol{x}-\boldsymbol{x}'}{|\boldsymbol{x}-\boldsymbol{x}'|^3}\,\mathrm{d}v'. \tag{3.32}$$

Note that, with a general current density function $\boldsymbol{J}$, not necessarily satisfying formula (3.10), instead of equation (3.25) we would have had

$$\nabla^2\boldsymbol{B} = -\mu_0\,\mathrm{curl}\,\boldsymbol{J} \tag{3.33}$$

[5] Formula (3.28) is derived from the general formula (see e.g. Jackson (1975)) $\mathrm{div}\,(f\boldsymbol{a}) = \boldsymbol{a}\cdot\mathrm{grad}\,f + f\mathrm{div}\boldsymbol{a}$ with $f = |\boldsymbol{x}-\boldsymbol{x}'|^{-1}$ and $\boldsymbol{a} = \boldsymbol{J}^i(\boldsymbol{x}')$.

[6] Formula (3.31) is derived from the general formula (see e.g. Jackson (1975)) $\mathrm{curl}(f\boldsymbol{a}) = \mathrm{grad}\,f\times\boldsymbol{a} + f\,\mathrm{curl}\boldsymbol{a}$ with $f = |\boldsymbol{x}-\boldsymbol{x}'|^{-1}$ and $\boldsymbol{a} = \boldsymbol{J}^i(\boldsymbol{x}')$.

a solution of which is, for a source $\boldsymbol{J}$ vanishing at infinity,

$$\boldsymbol{B}(\boldsymbol{x}) = \frac{\mu_0}{4\pi} \int \frac{\operatorname{curl}' \boldsymbol{J}(\boldsymbol{x}')}{|\boldsymbol{x} - \boldsymbol{x}'|} \, \mathrm{d}v' \tag{3.34}$$

and the same derivation leading to (3.32) would have yielded instead

$$\boldsymbol{B}(\boldsymbol{x}) = \frac{\mu_0}{4\pi} \int \boldsymbol{J}(\boldsymbol{x}') \times \frac{\boldsymbol{x} - \boldsymbol{x}'}{|\boldsymbol{x} - \boldsymbol{x}'|^3} \, \mathrm{d}v'. \tag{3.35}$$

It may be shown, by substituting formula (3.10) into (3.35), that the previous formula yields the same result as formula (3.32) in the case of an infinite homogeneous conductor. However formula (3.35) has general validity, including the case where (3.10) is satisified but the conductivity is nonhomogeneous. Formula (3.35) is also known as the Ampère–Laplace law, which is the current density counterpart of the Biot–Savart law for current carrying wires.

3.3. Magnetic field and electric potential for a piecewise homogeneous medium

Let us now consider a more realistic situation in which the volume conductor is bounded. To allow for tissue inhomogeneity, we consider now a conductivity function σ that may take different values inside the volume conductor. In the modelling of neuromagnetic fields we only need to take into account the organ-size-scale inhomogeneities of the head. Accordingly, we assume that the volume conductor is composed of regions of uniform conductivity. For simplicity, we further assume that any region of uniform conductivity is completely surrounded by another region of uniform conductivity. These regions would correspond, in data modelling, to one or more of the following tissues: scalp, skull, cerebrospinal fluid and brain. Finally, we assume that the impressed currents are confined to the innermost region.

Let then $V_K, V_{K-1}, \ldots, V_0$ be volumes in space satisfying the condition

$$V_K \supset V_{K-1} \supset \cdots \supset V_0 \tag{3.36}$$

and let S_j be the outer boundary of volume V_j. S_K is the boundary of the volume conductor, and the other surfaces S_j inside the volume conductor are boundaries between regions with different conductivities. Let σ_j be the conductivity of the region limited by the surfaces S_j and S_{j-1}. Note that this region corresponds to the volume $W_j = V_j - V_{j-1}$. Then σ_0 is the conductivity of the innermost region, and, since V_K is the external boundary of the volume conductor, $\sigma_{K+1} = 0$. The impressed current $\boldsymbol{J}^i$ is nonvanishing only inside V_0.

Proceeding as previously for the infinite homogeneous medium, from (3.22), using (3.23), and (3.16), we now obtain

$$\nabla^2 \boldsymbol{B} = -\mu_0(\operatorname{curl} \boldsymbol{J}^i + \operatorname{curl}(\sigma \boldsymbol{E})). \tag{3.37}$$

Comparing this equation with (3.25), we see that when the conductivity is not uniform the volume current contributes to the magnetic field through the term $\operatorname{curl}(\sigma \boldsymbol{E})$. In other words, the vortices of the volume current, caused by the inhomogeneities in conductivity, are additional sources of the magnetic field. In our idealized assumption of a piecewise uniform conductivity, the function $\sigma \boldsymbol{E}$ is curl free inside any homogenous region. Therefore, contributions to the magnetic field originate from the interfaces between these regions. To evaluate the source function on the interfaces let us imagine that σ varies smoothly over a very small thickness across the interface, so that $\boldsymbol{E}$ is also smooth. Then, using (3.15), we have the identity

$$\operatorname{curl}(\sigma \boldsymbol{E}) = \operatorname{grad} \sigma \times \boldsymbol{E}. \tag{3.38}$$

If we now let the region of finite thickness, across which σ varies, shrink to a surface, so that σ becomes a step function, we have

$$\operatorname{grad} \sigma = \Delta\sigma \, \delta(s(\boldsymbol{x}))\boldsymbol{n} \tag{3.39}$$

where $s(\boldsymbol{x}) = 0$ is an implicit representation of the discontinuity surface, $\boldsymbol{n}$ is a unit vector orthogonal to that surface and $\Delta\sigma$ is the conductivity step across that surface in the direction of $\boldsymbol{n}$. We may now use formula (3.39) to express the additional source term in equation (3.37):

$$\operatorname{curl}(\sigma \boldsymbol{E}) = -\sum_{j=0}^{K}(\sigma_{j+1} - \sigma_j)\delta(s_j(\boldsymbol{x}))\boldsymbol{n}_j \times \operatorname{grad}\Phi \tag{3.40}$$

where $s_j(\boldsymbol{x}) = 0$ is an implicit representation of surface S_j, $\boldsymbol{n}_j$ is a unit vector orthogonal to surface S_j, pointing outwards, and summation is extended over all surfaces S_j, for $j = 0, \ldots K$. Taking (3.40) into account, it may be shown that the solution of (3.37) is

$$\boldsymbol{B}(\boldsymbol{x}) = \boldsymbol{B}_\infty(\boldsymbol{x}) - \frac{\mu_0}{4\pi}\sum_{j=0}^{K}(\sigma_{j+1} - \sigma_j)\int_{S_j}\frac{\boldsymbol{n}'_j \times \operatorname{grad}'\Phi}{|\boldsymbol{x} - \boldsymbol{x}'|}\,\mathrm{d}a' \tag{3.41}$$

where $\boldsymbol{B}_\infty(\boldsymbol{x})$ is given by (3.27) and is the magnetic field generated by the impressed current as if the volume conductor were infinite and homogeneous. The integrals in the second term of the right-hand side of (3.41) are now taken over the interfaces and may be transformed using Stokes's theorem to yield (Geselowitz 1970)

$$\boldsymbol{B}(\boldsymbol{x}) = \boldsymbol{B}_\infty(\boldsymbol{x}) + \frac{\mu_0}{4\pi}\sum_{j=0}^{K}(\sigma_{j+1} - \sigma_j)\int_{S_j}\frac{\Phi\boldsymbol{n}'_j \times (\boldsymbol{x} - \boldsymbol{x}')}{|\boldsymbol{x} - \boldsymbol{x}'|^3}\,\mathrm{d}a'. \tag{3.42}$$

Comparing (3.42) with the Ampère–Laplace law (3.35), we see that the contribution of the interfaces between regions with different conductivity to the total magnetic field is equivalent to a current density $\Delta\sigma\,\Phi$ over the interfaces. Note that the direction of this current density is orthogonal to the interfaces rather than parallel to them. Note also that this current density is not real but fictitious; it is sometimes called the *secondary current* or *secondary source*.

From (3.42) we also note that, in a piecewise homogeneous medium, $\boldsymbol{B}$ depends on the value of Φ at the interfaces between homogeneous regions. Thus, to calculate the magnetic field we must first calculate the electric potential at the interfaces. We may find the electric potential by an argument similar to that leading to (3.40) and (3.42). When discontinuity surfaces are taken into account, equation (3.22) becomes

$$\sigma\nabla^2\Phi = \operatorname{div}\boldsymbol{J}^i - \sum_{j=0}^{K}(\sigma_{j+1} - \sigma_j)\delta(s_j(\boldsymbol{x}))\boldsymbol{n}_j \cdot \operatorname{grad}\Phi \tag{3.43}$$

where, again, $s_j(\boldsymbol{x}) = 0$ is an implicit representation of surface S_j, and $\boldsymbol{n}_j$ is a unit vector orthogonal to surface S_j, pointing outwards, and summation is extended over all surfaces S_j, for $j = 0, \ldots, K$.

It may be shown that, with this source function, the electric potential at a point $\boldsymbol{x}$, inside volume V_K but not lying on any of the interfaces S_j, is the solution of the following integral equation:

$$\sigma(\boldsymbol{x})\Phi(\boldsymbol{x}) = \sigma_0\Phi^0_\infty(\boldsymbol{x}) + \frac{1}{4\pi}\sum_{j=0}^{K}(\sigma_{j+1} - \sigma_j)\int_{S_j}\frac{\Phi(\boldsymbol{x}')\boldsymbol{n}'_j \cdot (\boldsymbol{x} - \boldsymbol{x}')}{|\boldsymbol{x} - \boldsymbol{x}'|^3}\,\mathrm{d}a' \tag{3.44}$$

where $\sigma(\boldsymbol{x})$ is the conductivity at point $\boldsymbol{x}$, and $\Phi^0_\infty(\boldsymbol{x})$ is the electric potential generated by the impressed current as if the medium were infinite and homogeneous with conductivity σ_0. The term $\sigma_0\Phi^0_\infty(\boldsymbol{x})$ is therefore given by (3.30) with $\sigma = 1$. Note that the effect of discontinuities in conductivity is represented by the electric potential generated by the same secondary source generating the magnetic field. If the point $\boldsymbol{x}$ lies on surface S_i, the singularity in the corresponding integral in the second term of the right-hand side of (3.44) must be taken

into account. The electric potential is then the solution of the following integral equation (Geselowitz 1967):

$$\frac{\sigma_{i+1}+\sigma_i}{2}\Phi_i(\boldsymbol{x}) = \sigma_0\Phi^0_\infty(\boldsymbol{x}) + \frac{1}{4\pi}\sum_{j=1}^{K}(\sigma_{j+1}-\sigma_j)\int_{S_j}\frac{\Phi(\boldsymbol{x}')\boldsymbol{n}'_j\cdot(\boldsymbol{x}-\boldsymbol{x}')}{|\boldsymbol{x}-\boldsymbol{x}'|^3}\,\mathrm{d}a' \tag{3.45}$$

where $i = 1, \ldots, K$, and the subscript in $\Phi_i(\boldsymbol{x})$ indicates that point $\boldsymbol{x}$ lies on surface S_i.

Note that

$$\mathrm{d}\Omega(\boldsymbol{x}, \boldsymbol{x}') = \boldsymbol{n}'\cdot(\boldsymbol{x}-\boldsymbol{x}')/|\boldsymbol{x}-\boldsymbol{x}'|^3\,\mathrm{d}a' \tag{3.46}$$

is the solid angle subtended at point $\boldsymbol{x}$ by an infinitesimal surface element $\boldsymbol{n}'\,\mathrm{d}a'$ at point $\boldsymbol{x}'$, so that equation (3.45) may be expressed as

$$\frac{\sigma_{i+1}+\sigma_i}{2}\Phi_i(\boldsymbol{x}) = \sigma_0\Phi^0_\infty(\boldsymbol{x}) + \frac{1}{4\pi}\sum_{j=1}^{K}(\sigma_{j+1}-\sigma_j)\int_{S_j}\Phi(\boldsymbol{x}')\,\mathrm{d}\Omega(\boldsymbol{x}, \boldsymbol{x}'). \tag{3.47}$$

4. The forward problem: modelling of source and volume conductor

In the previous section we reviewed the basic physical theory for the calculation of the magnetic field generated by an arbitrary current density flowing in a biological conductor. We considered two conductivity functions representing the volume conductor: homogeneous and piecewise homogenous functions. The first one is the simplest possible conductivity function and was used only to derive basic formulae and properties of the magnetic field. The second one is more realistic and practical, due to the compartmental nature of tissues in the human body. In this section we shall deal more specifically with modelling, i.e. with the calculation of the magnetic field generated by neural currents in particular situations, in the perspective of MEG data analysis. This modelling requires us to represent the volume conductor as well as the impressed currents. The first task in practice reduces to the specialization of formula (3.42)—and, if necessary, of equation (3.45)—to specific conductor geometries, with either analytical or numerical description. The second task is necessary in order to reduce the number of parameters that characterize the current density to be inferred from magnetic field measurements, as will be described in the next section. We shall first describe the most frequently used source models, and then turn to the volume conductor models: the homogeneous spherical model, for which an analytical expression of the magnetic field is possible, and a realistic model, that uses numerically represented surfaces and the boundary element method (BEM) to calculate the magnetic field.

4.1. Source modelling

The basic element used to model neural electric currents is the current dipole. It may be viewed as a short element of current, characterized by an intensity I of the current, and a vector $\boldsymbol{L}$, indicating the direction and the length of the element. The current dipole moment $\boldsymbol{Q}$ is defined as

$$\boldsymbol{Q} = I\boldsymbol{L}. \tag{4.1}$$

The current dipole is a pointlike source that is obtained by letting $I \to \infty$ and $\boldsymbol{L} \to 0$, while $\boldsymbol{Q}$ remains constant. The current density corresponding to a current dipole located at point $\boldsymbol{x}_0$ is

$$\boldsymbol{J}^i(\boldsymbol{x}) = \boldsymbol{Q}\delta(\boldsymbol{x}-\boldsymbol{x}_0). \tag{4.2}$$

The current dipole alone does not satisfy the law of conservation of charge (3.19). The latter is satisfied when the volume current is included in the total current $\boldsymbol{J}(\boldsymbol{x})$ according to (3.10). Another point of view on the current dipole is that of a source and a sink of current of equal intensity I that are displaced by a distance $\boldsymbol{L}$. The resulting current density is in fact the volume current density, while the current dipole connects the sink with the source, thereby assuring the conservation of charge. By substituting formula (4.2) into (3.30) and (3.32) we obtain the electric potential and the magnetic field of a current dipole located at point $\boldsymbol{x}_0$ in an infinite homogeneously conducting medium:

$$\Phi_\infty(\boldsymbol{x}) = \frac{1}{4\pi\sigma}\boldsymbol{Q}\cdot\frac{\boldsymbol{x}-\boldsymbol{x}_0}{|\boldsymbol{x}-\boldsymbol{x}_0|^3} \tag{4.3}$$

$$\boldsymbol{B}_\infty(\boldsymbol{x}) = \frac{\mu_0}{4\pi}\boldsymbol{Q}\times\frac{\boldsymbol{x}-\boldsymbol{x}_0}{|\boldsymbol{x}-\boldsymbol{x}_0|^3}. \tag{4.4}$$

The SI unit of current dipole moment is the ampère-metre (A m).

4.1.1. The microscopic current dipole model. We shall now give an estimate of the order of magnitude of the current dipole moment associated with an 'elementary' neural current. In section 2 we briefly reviewed the mechanisms of active cell electric communication via action potentials and postsynaptic potentials. It is the latter that mainly contributes to the MEG signals, as will be argued in the following. Strictly speaking, only transmembrane currents are impressed currents. However, due to the high electrical resistance of the cell membrane that isolates electrically the intracellular from the extracellular medium, it is practical to include the intracellular current in the impressed current. Actually, since the contribution to the magnetic field of the transmembrane current can be shown to be negligible, it is the intracellular current that we take as representative of the electric activity of the cell. In the case of a postsynaptic potential, the current flowing in a dendrite may be modelled as a current dipole, the moment of which may be expressed as (Tripp 1983)

$$Q = \sigma A \Delta\Phi \tag{4.5}$$

where σ is the conductivity of the intracellular medium, A is the cross-sectional area of the dendrite and $\Delta\Phi$ is the potential difference along the dendrite. Inserting typical values into (4.5) yields an estimate of the order of magnitude of Q for a single postsynaptic potential. If we consider a dendrite 1 μm in diameter, $\sigma = 0.25\ \Omega^{-1}\ \mathrm{m}^{-1}$, $\Delta\Phi = 10$ mV, we obtain $Q = 2\times10^{-15}$ A m. In turn, with this value of current dipole moment, from formula (4.4) we obtain the intensity of the magnetic field generated by a postsynaptic potential at a five centimetre distance: $B = 8\times10^{-20}$ T. This field is about six orders of magnitude smaller than the field actually measured over the scalp in typical evoked magnetic field recordings. On one hand, this shows that MEG signals correspond to the simultaneous or synchronizsed firing of large assemblies of neurons, corresponding to about 1000 000 synapses. On the other hand, the above view of the current dipole representing the activity of a single neuron is not applicable to MEG data interpretation. In other words MEG only allows the investigation of brain electrical activity at the macroscopic level. There is, however, another use for the current dipole model.

4.1.2. The macroscopic current dipole model. The current density of (4.2) may be used to represent a small portion of cerebral tissue where a large number of neurons are firing synchronously. The size of such a portion of tissue is indeed small compared with the distance to the point where the magnetic field is measured, since 1 mm^2 of cortex may contain as many as 10^8 synapses. In this case, the current dipole moment may be viewed as the vector sum of all

microscopic current dipoles in the active region. A macroscopic current dipole is often called an equivalent current dipole (ECD). If $\boldsymbol{J}^i(\boldsymbol{x})$ is the actual impressed current density function, the moment of the ECD may be expressed as

$$\boldsymbol{Q} = \int \boldsymbol{J}^i(\boldsymbol{x}')\,\mathrm{d}v' \tag{4.6}$$

where the integral is extended over the volume of the active region. The intensity of the ECD moment is in principle roughly proportional to the number of active neurons. However, if the active region has a complex shape, for example a folded region in a cortical gyrus, cancellation of microscopic dipoles with opposite directions may contradict this rule. For neurons located in the cortex, the prevailing orientation of the dendrites where the postsynaptic potentials occur is perpendicular to the cortex surface. Therefore, the orientation of the ECD moment is in principle also perpendicular to the surface. Here again, a complex shape of the active region may lead to deviations from this rule. These considerations show that any information on the structure of the active region is lost in the ECD model. This is the price paid in the adoption of a simple model. More complex models may be used if the shape of the region is a concern.

4.1.3. Extended sources. In reality, no source is pointlike since it comprises a large number of neurons. In practice, some field patterns are well fitted by an ECD (see the next section on the inverse problem solution) that contains only information on the position of the source and on its orientation, whereas other field patterns are more complex, and the assumption of a dipolar source may yield a bad-quality fit with estimated parameters that have no link with reality. In this case, a more complex model may be able to reconstruct more closely the measured field pattern, and therefore yield a reliable estimate of source position. Alternatively, the researcher may have a direct interest in finding information, in addition to the position parameters, that reflects the shape and the extension of the source. The multipole expansion is a series expansion of the magnetic field $\boldsymbol{B}(\boldsymbol{x})$, generated at point $\boldsymbol{x}$ outside the volume conductor, in terms of the primary current density $\boldsymbol{J}^i(\boldsymbol{x}'')$, assuming that the latter is confined to a small volume around a point $\boldsymbol{x}'$. The zeroth moment of the multipole expansion is the ECD given by (4.6). The first moment is the 3×3 current quadrupole tensor $\boldsymbol{A}$, the elements of which are given by

$$A_{jk} = \int x_j'' J_k^i(\boldsymbol{x}'')\,\mathrm{d}v'' \tag{4.7}$$

where $j, k = 1, 2, 3$ indicate the three axes of the coordinate system. As an example of the corresponding magnetic field expression we indicate the contribution of the first moment to the third component of the magnetic field (Katila and Karp 1983):

$$B_3^{(1)}(\boldsymbol{x}) = \frac{\mu_0}{4\pi|\boldsymbol{x}|^5}[3x_2(x_1A_{11} + x_2A_{21} + x_3A_{31}) - 3x_1(x_1A_{12} + x_2A_{22} + x_3A_{32}) + |\boldsymbol{x}|^2(A_{12} - A_{21})]. \tag{4.8}$$

This formula only gives the contribution of the primary current density, and is therefore valid only if the volume current contribution may be neglected. The complete calculation of the magnetic field would require first the calculation of the electric potential distribution on the interfaces between homogeneous compartments of the volume conductor. Alternatively, as was recently proposed by Nolte and Curio (1997), the field of a quadrupole source may be obtained by appropriately differentiating a dipole field that already takes into account the volume current contribution, thereby greatly simplifying the calculations.

4.2. The spherical volume conductor model

We now turn to volume conductor modelling. A simple model that allows an analytical expression for the magnetic field is a bounded conductor with a spherically symmetric conductivity function. This includes as a special case the homogeneously conducting sphere. We shall assume that the conductivity is piecewise homogeneous and consider an arbitrary impressed current density $\boldsymbol{J}^i(\boldsymbol{x})$. The magnetic field generated outside the sphere is given by formula (3.42), where now the origin of the coordinate system is taken at the centre of the sphere:

$$\boldsymbol{B}(\boldsymbol{x}) = \boldsymbol{B}_\infty(\boldsymbol{x}) + \frac{\mu_0}{4\pi}\sum_{j=0}^{K}(\sigma_{j+1}-\sigma_j)\int_{S_j}\frac{\Phi\boldsymbol{n}'_j\times(\boldsymbol{x}-\boldsymbol{x}')}{|\boldsymbol{x}-\boldsymbol{x}'|^3}\,\mathrm{d}a'. \tag{4.9}$$

If $\boldsymbol{e}_r$ is a radially oriented unit vector at point $\boldsymbol{x}$, then $B_r(\boldsymbol{x}) = \boldsymbol{B}(\boldsymbol{x})\cdot\boldsymbol{e}_r$ is the radial component of the magnetic field at point $\boldsymbol{x}$:

$$B_r(\boldsymbol{x}) = \boldsymbol{B}_\infty(\boldsymbol{x})\cdot\boldsymbol{e}_r + \frac{\mu_0}{4\pi}\sum_{j=0}^{K}(\sigma_{j+1}-\sigma_j)\int_{S_j}\frac{\Phi\boldsymbol{n}'_j\times(\boldsymbol{x}-\boldsymbol{x}')\cdot\boldsymbol{e}_r}{|\boldsymbol{x}-\boldsymbol{x}'|^3}\,\mathrm{d}a'. \tag{4.10}$$

Note that, since $\boldsymbol{n}'_j$ is a unit vector at point $\boldsymbol{x}'$ orthogonal to the spherical surface S_j, the three vectors in the numerator of the integrands on the right-hand side of (4.10) lie in a plane, so that their mixed product vanishes identically over the surface of integration. Therefore, the contribution of volume current vanishes, and the radial component of the magnetic field is given by

$$B_r(\boldsymbol{x}) = \frac{\mu_0}{4\pi}\int\frac{\boldsymbol{J}^i(\boldsymbol{x}')\times(\boldsymbol{x}-\boldsymbol{x}')\cdot\boldsymbol{e}_r}{|\boldsymbol{x}-\boldsymbol{x}'|^3}\,\mathrm{d}v'. \tag{4.11}$$

Note that the contribution of volume current to the total magnetic field is not vanishing. It is tangential to the surface of the sphere as may be seen from the numerator of the integrands in (4.9). We shall now calculate the total magnetic field when the source is a current dipole. From (3.16) it follows that, outside the volume conductor,

$$\boldsymbol{B} = -\mathrm{grad}\,\Phi_m \tag{4.12}$$

where Φ_m is the scalar magnetic potential. Since the conductor is bounded, Φ_m may be assumed to vanish at infinity, so

$$\Phi_m(\boldsymbol{x}) = \int_{|\boldsymbol{x}|}^{\infty} B_r(\boldsymbol{x})\,\mathrm{d}r' \tag{4.13}$$

where the line integral is taken along a radial path from point $\boldsymbol{x}$ to infinity. Note that, since for any piecewise spherically symmetric conductivity function B_r is given by (4.11), Φ_m, and hence $\boldsymbol{B}$, do not depend on the conductivity. Therefore, any spherically symmetric volume conductor is equivalent to a homogeneous sphere. If the source is a current dipole at point $\boldsymbol{x}_0$, the radial component of the magnetic field is

$$B_r(\boldsymbol{x}) = \frac{\mu_0}{4\pi}\frac{\boldsymbol{Q}\times(\boldsymbol{x}-\boldsymbol{x}_0)\cdot\boldsymbol{e}_r}{|\boldsymbol{x}-\boldsymbol{x}_0|^3} \tag{4.14}$$

and by using (4.13) and (4.12) we obtain the magnetic field of a current dipole in a homogeneous sphere (Ilmoniemi *et al* 1985, Sarvas 1987):

$$\boldsymbol{B}(\boldsymbol{x}) = \frac{\mu_0}{4\pi F}(F\boldsymbol{Q}\times\boldsymbol{x}_0 - \boldsymbol{Q}\times\boldsymbol{x}_0\cdot\boldsymbol{x}\,\mathrm{grad}\,F) \tag{4.15}$$

where

$$F = a(ax + \boldsymbol{a} \cdot \boldsymbol{x}) \tag{4.16}$$

$$\boldsymbol{a} = \boldsymbol{x} - \boldsymbol{x}_0 \tag{4.17}$$

$$\text{grad } F = (x^{-1}a^2 + a^{-1}\boldsymbol{a} \cdot \boldsymbol{x} + 2a + 2x)\boldsymbol{x} - (a + 2x + a^{-1}\boldsymbol{a} \cdot \boldsymbol{x})\boldsymbol{x}_0. \tag{4.18}$$

Note that (4.15) gives the total magnetic field, i.e. the sum of primary and secondary current contributions. Note also that a radially oriented current dipole does not generate any field outside the sphere, since $\boldsymbol{Q} \times \boldsymbol{x}_0$ vanishes. The latter result may also be obtained from the Ampère theorem and the symmetry of the problem about the current dipole axis. Some of the results obtained in the above derivation, although strictly valid only for a spherical head, give us an indication of the qualitative features of the neuromagnetic field. In particular, we have the following.

(1) The component of the magnetic field orthogonal to the surface of the volume conductor is weakly dependent on volume currents.
(2) The magnetic field generated by a current dipole oriented orthogonally to the volume conductor surface is weak, so MEG is mostly sensitive to tangential current dipoles. Since dendrites are mostly orthogonal to the cortical surface, MEG is mostly sensitive to sources located in the fissures of the cortex.
(3) The formula (4.14) is a good approximation of the measured field when the sensors are oriented in such a way that they measure the orthogonal component of the magnetic field. We shall use this formula to give an insight into the magnetic field pattern of a dipolar source. It is useful to transform (4.14) into polar coordinates:

$$B_r(\theta, \varphi) = \frac{\mu_0 Q[(R/d) - 1] \sin\theta \cos\theta \sin\varphi}{4\pi d^2[((R/d)^2 - 1) \sin 2\theta + 1]^{3/2}}. \tag{4.19}$$

Formula (4.19) gives the radial component of the magnetic field generated at a spherical surface of radius R by a current dipole of moment Q located at a depth d below the surface, on the z-axis, and oriented along the positive direction of the x-axis. θ and φ are the usual polar angles and the origin of coordiantes is at the centre of the sphere. We can see that the magnetic field is antisymmetric with respect to the xz-plane that contains the dipole, and is zero in that plane. If we consider the variations of B_r in a plane orthogonal to the dipole, we can see that it is extremal at an angle θ_m that does not depend on the current dipole moment. Therefore B_r has a maximum and a minimum, with the current dipole lying midway between them. θ_m may be found by differentiation of (4.19), and is roughly proportional to current dipole depth, for shallow current dipoles, while it increases more slowly for deeper current dipoles. Formula (4.19) is useful because it illustrates the characteristic field pattern of a current dipole. In some cases the mere inspection of a magnetic field map at a particular instant may give a clue as to where the field generators are located.

4.3. A realistic volume conductor model: the boundary element method (BEM)

In some areas, in particular the temporal areas, the head markedly deviates from a spherical shape. Realistic models allow us to take into account the real shape of the head. We shall limit the description of realistic models to the case of piecewise homogeneous volume conductors. When the interfaces between homogeneous regions have an arbitrary shape they must be given a numerical representation. This is in practice a list of points lying on the interfaces, that is typically obtained from an MRI by means of segmentation techniques that isolate the different homogeneous regions in the head. It is not possible in general to find a closed analytical expression for the magnetic field, as in the case of the homogeneous sphere (4.15). Therefore,

the electric potential at the interface must be first obtained, by solving equation (3.47), and then the volume current contribution may be calculated using formula (3.42). Due to the numerical representation of the interfaces, both problems must be addressed by discretizing the integrals in (3.47) and (3.42). This is done by approximating each interface by a set of contiguous triangular panels, then by solving (3.47) for the electric potential at the centroid of each triangle, and finally by calculating the volume current contribution according to (3.42). This technique is referred to as the BEM. The discretized version of equation (3.47) is

$$\Phi_i^m = \frac{2\sigma_0}{(\sigma_i + \sigma_{i+1})}\Phi_{0\infty i}^m + \frac{1}{2\pi}\sum_{j=0}^{K}\sum_{n=1}^{N_j}\frac{(\sigma_j - \sigma_{j+1})}{(\sigma_i + \sigma_{i+1})}\Omega_{ij}^{mn}\Phi_j^n \tag{4.20}$$

where Φ_i^m is the electric potential at the centroid of the mth triangle on the ith surface, Ω_{ij}^{mn} is the solid angle subtended at the centroid of the mth triangle on the ith surface by the nth triangle on the jth surface and $\Phi_{0\infty i}^m$ is the electric potential that would be generated by the primary current at the centroid of the mth triangle on the ith surface if the medium were infinite homogeneous with conductivity σ_0. The index n runs over the N_j triangles of the jth surface, and the total number of triangles is given by

$$N_T = \sum_{j=0}^{K} N_j. \tag{4.21}$$

Ω_{ij}^{mn} may be calculated according to a formula by Oosterom and Strackee (1983), and $\Omega_{ii}^{mm} = 0$. $\Phi_{0\infty i}^m$ is given by formula (3.30) for the general case, or by formula (4.3) for the case of a single ECD. Equation (4.20) may be expressed in matrix form:

$$\boldsymbol{\Phi} = \boldsymbol{D} + \underline{\boldsymbol{E}}\boldsymbol{\Phi} \tag{4.22}$$

where $\boldsymbol{\Phi}$ is a column vector the N_T components of which are the values of the electric potential at all centroids, $\boldsymbol{D}$ is a column vector the N_T components of which are the first terms in the right-hand side of (4.20) and $\underline{\boldsymbol{E}}$ is a $N_T \times N_T$ matrix the elements of which are

$$E_{ij}^{mn} = \frac{(\sigma_j - \sigma_{j+1})}{2\pi(\sigma_i + \sigma_{i+1})}\Omega_{ij}^{mn} \tag{4.23a}$$

$$E_{ii}^{mm} = 0. \tag{4.23b}$$

The matrix $\underline{\boldsymbol{E}}$ depends only on the conductivities of the medium and on the solid angles Ω_{ij}^{mn}. Therefore it depends only on the model and not on the sources.

Equation (4.22) may be rewritten as

$$(\underline{\boldsymbol{I}} - \underline{\boldsymbol{E}})\boldsymbol{\Phi} = \boldsymbol{D} \tag{4.24}$$

where $\underline{\boldsymbol{I}}$ is the identity matrix. The matrix $(\underline{\boldsymbol{I}} - \underline{\boldsymbol{E}})$ is singular, corresponding to the fact that the potential is only defined up to an additive constant. The singularity may be removed by a procedure called deflation (Barnard *et al* 1967, Lynn and Timlake 1968). Finally, the solution for the electric potential may be found by direct inversion of the deflated matrix (Oostendorp and Oosterom 1989). Once the electric potential at the centroids of all triangles is known, the magnetic field may be calculated by means of formula (3.42). Note that, due to the discretization of the problem, the continuous current dipole density over the interfaces between media of different conductivity is replaced by a discrete array of current dipoles—one at the centroid of each triangle—the moments of which are given by

$$\boldsymbol{Q}_j^n = (\sigma_{j+1} - \sigma_j)\Phi_j^n a_j^n \boldsymbol{n}_j^n \tag{4.25}$$

where, as before, the index j runs over the surfaces of the model, and the index n runs over the triangles of a surface. a_j^n is the area of triangle (j, n) and $\boldsymbol{n}_j^n$ is a unit vector orthogonal to

the triangle and pointing to the exterior of the surface. Denoting by $\boldsymbol{x}_j^n$ the position vector of the centroid of triangle (j, n) the discretization of (3.42) yields

$$\boldsymbol{B}(\boldsymbol{x}) = \boldsymbol{B}_\infty(\boldsymbol{x}) + \frac{\mu_0}{4\pi}\sum_{j=0}^{K}(\sigma_{j+1} - \sigma_j)\sum_{n=1}^{N_j}\frac{\Phi_j^n a_j^n \boldsymbol{n}_j^n \times (\boldsymbol{x} - \boldsymbol{x}_j^n)}{|\boldsymbol{x} - \boldsymbol{x}_j^n|^3} \tag{4.26}$$

where $\boldsymbol{B}_\infty(\boldsymbol{x})$ is given by (3.32) for the general case, and by (4.4) for the case of a single ECD.

In order to take into account the major tissue inhomogeneities, a numerical head would comprise three surfaces: the scalp–air interface, the scalp–skull interface and the skull–brain interface. The conductivities of scalp and brain are assumed to be equal, while the conductivity of the skull is about one hundred times smaller. The presence of a layer with low conductivity between the brain and the scalp is responsible for the poor accuracy formerly obtained with the BEM. The reason for this was pointed out by Hämäläinen and Sarvas (1989), and may be appreciated if equation (4.22) is decomposed into blocks:

$$\boldsymbol{\Phi}_1 = \underline{\boldsymbol{E}}_{11}\boldsymbol{\Phi}_1 + \underline{\boldsymbol{E}}_{12}\boldsymbol{\Phi}_2 + \underline{\boldsymbol{E}}_{13}\boldsymbol{\Phi}_3 + \boldsymbol{D}_1 \tag{4.27a}$$

$$\boldsymbol{\Phi}_2 = \underline{\boldsymbol{E}}_{21}\Phi_1 + \underline{\boldsymbol{E}}_{22}\boldsymbol{\Phi}_2 + \underline{\boldsymbol{E}}_{23}\boldsymbol{\Phi}_3 + \boldsymbol{D}_2 \tag{4.27b}$$

$$\boldsymbol{\Phi}_3 = \underline{\boldsymbol{E}}_{31}\boldsymbol{\Phi}_1 + \underline{\boldsymbol{E}}_{32}\boldsymbol{\Phi}_2 + \underline{\boldsymbol{E}}_{33}\boldsymbol{\Phi}_3 + \boldsymbol{D}_3 \tag{4.27c}$$

where the indices 1, 2 and 3 indicate the three interfaces described above, in the same order. Due to the low conductivity of the skull, the electric potential over the scalp–air and over the skull–scalp interfaces is much smaller than that at the brain–skull interface. Therefore, the elements in vectors $\boldsymbol{\Phi}_1$ and $\boldsymbol{\Phi}_2$ are much smaller than those in vector $\boldsymbol{\Phi}_3$. In equations (4.27*a*) and (4.27*b*), the small values of $\boldsymbol{\Phi}_j$ $(j = 1, 2)$ are the result of cancellations between two large terms, $\underline{\boldsymbol{E}}_{j3}\boldsymbol{\Phi}_3$ and $\boldsymbol{D}_j$, and inaccuracies in $\boldsymbol{\Phi}_3$ propagate into $\boldsymbol{\Phi}_1$ and $\boldsymbol{\Phi}_2$, leading to high relative errors in these vectors. Hämäläinen and Sarvas (1989) have proposed circumventing this difficulty by seeking the solution in the form $(j = 1, 2, 3)$

$$\boldsymbol{\Phi}_j = \boldsymbol{\Psi}_j^0 + \boldsymbol{\Psi}_j \tag{4.28}$$

where $\boldsymbol{\Psi}_j^0$ is the solution for the same model, but with a vanishing skull conductivity. In this case, $\boldsymbol{\Psi}_1^0 = \boldsymbol{\Psi}_2^0 = 0$, and $\boldsymbol{\Psi}_3^0$ is first found by solving (4.20) for a homogeneous volume conductor consisting only of the innermost region and surface of the previous three-compartment model. The vectors $\boldsymbol{\Psi}_j (j = 1, 2, 3)$ are then found by solving a system of equations similar to (4.27):

$$\boldsymbol{\Psi}_1 = \underline{\boldsymbol{E}}_{11}\Psi_1 + \underline{\boldsymbol{E}}_{12}\Psi_2 + \underline{\boldsymbol{E}}_{13}\Psi_3 + \boldsymbol{F}_1 \tag{4.29a}$$

$$\boldsymbol{\Psi}_2 = \underline{\boldsymbol{E}}_{21}\Psi_1 + \underline{\boldsymbol{E}}_{22}\Psi_2 + \underline{\boldsymbol{E}}_{23}\Psi_3 + \boldsymbol{F}_2 \tag{4.29b}$$

$$\boldsymbol{\Psi}_3 = \underline{\boldsymbol{E}}_{31}\Psi_1 + \underline{\boldsymbol{E}}_{32}\Psi_2 + \underline{\boldsymbol{E}}_{33}\Psi_3 + \boldsymbol{F}_3 \tag{4.29c}$$

where the vector $\boldsymbol{F}_3$ depends on $\boldsymbol{\Psi}_3^0$. This method, called the isolated problem approach, although it requires an additional matrix inversion, allows one to compute the potential accurately. The increase in the number of triangles required to obtain the same increase in accuracy would raise the computational costs much more. It is important to use this method when the calculation is aimed at finding the electric potential over the scalp. However, in MEG, the magnetic field is the final target. Hämäläinen and Sarvas (1989) have shown that, due to the small value of the electric potential on the air–scalp and scalp–skull interfaces, the corresponding terms contributing to the magnetic field in formulae (3.42) or (4.26) may be neglected without an appreciable loss in accuracy. An interpretation of this fact in terms of volume current density is that the latter is mostly confined inside the brain. Therefore, the three-compartment model may be replaced in MEG by the homogeneous model, thereby reducing the computational costs.

An alternative implementation of the BEM model uses the vertices of the triangles, rather than the centroids, as the points where the electric potential is calculated. It is called the node-based BEM, and its advantage lies in the fact that a triangulated surface contains about half as many vertices as triangles, thereby reducing the computational cost. While the centroid-based BEM assumes that the electric potential is constant over a triangle, this is not possible in the node-based BEM. In the latter case, it is usually assumed that the potential varies linearly over a triangle. In the node-based BEM, the discretization of equation (3.47) differs from that sketched above for the centroid-based BEM. For example, the solid angle matrix element connecting a node with another one is now calculated using all the triangles around one of the nodes. The analytical calculations involved in the discretization of (3.47) have been described by Munck (1992). The calculation of the magnetic field and the discretization of (3.42) is also different since the variations of the electric potential over a triangle must be taken into account. This aspect has been treated by Ferguson *et al* (1994).

5. The inverse problem: reconstruction of neural sources

After having reviewed the most common head models used for the forward-problem solution in MEG, we turn to a description of some of the methods for the solution of the inverse problem—i.e. the inference of neural current sources from magnetic field measurements over the scalp—which is the goal of MEG. As already mentioned in section 2, the bioelectromagnetic inverse problem has no unique solution. This was first observed by Helmholtz in 1853. Mathematically, this may be understood as a consequence of the existence of silent sources. For example, a radial current dipole in a homogeneously conducting sphere, seen in section 4, is a magnetically silent source. Thus, the addition of a silent source to a solution of a particular neuromagnetic inverse problem yields another solution of the same problem. Therefore, to find a practical solution in any particular case, the variability of the source is usually restricted. There are principally two ways to do this. One is to assume a source model that is characterized by a small number of parameters so that the specification of the magnetic field at a sufficient number of points in space defines the source uniquely. Examples of such models are the single or multiple ECD, or the multipole expansion. The second involves assuming a more complex source model, allowing a larger variability, and then imposing constraints on the solution so that it is the unique solution satisfying a prescribed criterion. Usually, the source model used in this case is a current dipole field, i.e. an array of a large number of current dipoles with fixed position. The problem is then a linear one, since only the momenta of the current dipoles must be found. Therefore the methods of linear inverse estimation are used. To these different models correspond different techniques for the solution of the inverse problem.

Before describing a number of inverse procedures, we should like to clarify a point that, although straightforward, must be taken into account in neural source reconstruction. For the sake of generality, the formulae in section 4 give the magnetic field at a measurement point. However, a piece of data always consists of a scalar quantity. In fact, as will be described in section 6, the output of each channel of a neuromagnetometer is proportional to the net magnetic flux through the flux transformer that couples the SQUID to the outside world. If the flux transformer consists of several coils, the net flux may be expressed as the (algebraic) sum of the mean orthogonal component of the magnetic field at each coil, multiplied by the area of that coil and by the number of turns in that coil. In any case, the output of each channel may be obtained by integrating the formulae for the magnetic field, to calculate the net magnetic flux. Note that, since the magnetic field depends linearly on the current density, so does the actual measured quantity. In order to implement an inverse problem solution procedure,

the dependence of the actual measured quantity on the source parameters must be calculated according to the particular instrument geometry.

5.1. Single-current-dipole solutions

If only one source is presumed to be active during a particular time interval, for example in the activation of the primary sensory–motor areas at particular latencies after stimulus presentation, a single ECD may be a suitable source model. In this case, formulae (4.13) or (4.24) for a spherical or a realistic volume conductor respectively, are used to calculate the magnetic field. Then the six parameters—three coordinates of position and three components of dipole moment—of the ECD are obtained by a least-squares fit between the measured and the theoretical field values. Note that, in the case of a spherical head model, only the two tangential components of the current dipole moment generate a magnetic field, so that five parameters describe the model completely. Since the magnetic field depends nonlinearly on the ECD position, the best-fit parameters are found by means of an iterative procedure such as the Levenberg–Marquardt algorithm (Marquardt 1963) or the simplex algorithm (Nelder and Mead 1965). It is possible to find the linear parameters at each step of this search by means of a linear fit, assuming for the ECD position coordinates the current values of the corresponding parameters. In this way the dimension of the parameter space is reduced. The main pitfall of iterative minimization algorithms is that they may become trapped in a local minimum. The validity of the fit may be evaluated by calculating the minimized residual:

$$R_{\min} = \sum_{j=1}^{M} (b_j^m - b_j)^2 / \sigma_j^2 \tag{5.1}$$

where b_j^m is the measured magnetic field value at sensor number j, σ_j is an estimate of the noise on this measurement and b_j is the theoretical magnetic field value at sensor number j. In the assumption of normally distributed noise, R is distributed like a chi-squared function with the appropriate number of degrees of freedom, so confidence limits for the model parameters may be found by standard methods. However the assumption of normally distributed noise is not quite justified in neuromagnetic measurements. Indeed, the main source of error is the uncertainty in sensor positioning. It is therefore more appropriate to evaluate the actual noise distribution of the measurement process, and to find confidence limits on the parameters by means of a Monte Carlo simulation.

In the single-current-dipole fit, the ECD parameters may be sought for at each instant of a selected part of the recorded time course. In this case, the parameter values at each instant are considered as independent from those at all other instants. For this reason, this procedure is often called a 'moving dipole' fit. Referring to the spherical head model, if the number of time samples is $\mathcal{T}$, the total number of parameters to be estimated is $5\mathcal{T}$. Physiologically, it may not be a sound assumption that ECD parameters at successive instants are completely independent. Moreover, small-scale variations in ECD position in a moving dipole fit may not be significant. Therefore, the experimenter may seek only one location for the cerebral activity related to a particular waveform in the MEG time course. In this case she would perform a 'fixed dipole' fit, in which the position of the ECD is assumed to be fixed—but unknown—throughout the τ time samples. The moment of the ECD may be of two kinds: it may have a fixed—but unknown—direction, in which case the intensity at each time sample is sufficient to describe the time course of the ECD, resulting in a total of $4 + \mathcal{T}$ parameters to be retrieved in the case of a spherical head model; or it may have a variable direction, in which case two components of the current dipole moment at each time sample are necessary to describe the time course of the ECD, resulting in a total of $3 + 2\mathcal{T}$ parameters to be retrieved, again in the case of a

spherical head model. The advantage of a fixed-dipole model over a moving-dipole model is that fewer parameters are obtained from the same set of data. In fact, it is not strictly necessary that only one source is active to use the single ECD model. In some cases, when several sources are simultaneously active, but are sufficiently shallow, and distant from each other, so that their field patterns do not overlap, single ECDs may be fitted separately to distinct parts of the magnetic field map.

5.2. Multiple-current-dipole solutions

Conversely, if two sources are simultaneously active, that are close to each other, or such that one of them has a rather extended field pattern, so that their field patterns overlap, a multiple-ECD model must be used to localize the sources. The procedure then becomes quite complex due to the increase in the number of parameters of the model. In addition, multiple moving ECDs may be unpractical. In fact, the overlapping of the field patterns may make it difficult to disentangle the single sources, even with a multiple-ECD model. For this reason, fixed ECDs are usually employed in multiple-ECD fits. Indeed, in addition to a reduced number of parameters, fixed-ECD models may benefit from the fact that different sources usually have different time courses. Thus, temporal information contained in the data time course may be used to complement spatial information contained in the maps. Fixed ECDs may again be of two types: with fixed or variable orientation. This procedure was first proposed by Scherg and Cramon for the analysis of EEG data, with some restrictions on the possible waveforms of the ECDs. A review of their work was published by Scherg (1991). The method was then generalized by Munck (1990) to ECDs with arbitrary waveforms.

The magnetic field component at any measurement site is a linear combination of all the current dipole components in the source model. This may be expressed in the following matrix form:

$$\boldsymbol{b} = \boldsymbol{A}\boldsymbol{q} \tag{5.2}$$

where $\boldsymbol{b}$ is an $M \times T$ matrix, $\boldsymbol{A}$ is an $M \times N$ matrix and $\boldsymbol{q}$ is an $N \times T$ matrix. A row of $\boldsymbol{b}$ represents the magnetic field theoretical time course, with τ samples, at one of the M sensor positions, while a column of $\boldsymbol{b}$ represents a theoretical magnetic field map at a particular time instant. Similarly, a row of $\boldsymbol{q}$ represents the time course of one of the N current dipole components. $\boldsymbol{A}$ is a transfer matrix, the ith column of which represents the magnetic field map that is generated when the ith dipole component is equal to unity, and all the others vanish. Note that the elements of $\boldsymbol{A}$ depend on sensor position as well as on current dipole position, so both $\boldsymbol{A}$ and $\boldsymbol{q}$ must be found by minimizing the sum of squared residuals over all sensors and time instants. If $\boldsymbol{b}^m$ is the matrix of measured magnetic field values, the residual may be expressed as

$$R = \sum_{j=1}^{M}\sum_{k=1}^{T}(b_{jk}^m - b_{jk})^2 = \mathrm{Tr}([\boldsymbol{b}^m - \boldsymbol{b}]^t[\boldsymbol{b}^m - \boldsymbol{b}]) = \|\boldsymbol{b}^m - \boldsymbol{A}\boldsymbol{q}\|^2 \tag{5.3}$$

where Tr denotes the trace of a matrix, t its transpose and $\| \|$ its Frobenius norm. Since the residual depends nonlinearly on current dipole position parameters, the minimization of R entails an iterative search in parameter space that is computationally demanding, and prone to instabilities, due to the large number of parameters. In some implementations, the ECD positions were assumed to be known on physiological grounds, thus eliminating the need for an iterative search. In this case the matrix containing the estimated time courses of the ECDs is given by

$$\boldsymbol{q}_{\mathrm{est}} = \boldsymbol{A}^{+}\boldsymbol{b}^m = (\boldsymbol{A}^t\boldsymbol{A})^{-1}\boldsymbol{A}^t\boldsymbol{b}^m \tag{5.4}$$

where $\boldsymbol{A}^+$ is the Moore–Penrose pseudoinverse of matrix $\boldsymbol{A}$. $\boldsymbol{A}\boldsymbol{q}_{\text{est}}$ is the projection of $\boldsymbol{b}^m$ onto the subspace spanned by the columns of $\boldsymbol{A}$:

$$\boldsymbol{A}\boldsymbol{q}_{\text{est}} = \boldsymbol{A}\boldsymbol{A}^+\boldsymbol{b}^m = \boldsymbol{P}_{\|}\boldsymbol{b}^m \tag{5.5}$$

and the minimized residual is given by

$$R_{\min} = \|(\boldsymbol{I} - \boldsymbol{A}\boldsymbol{A}^+)\boldsymbol{b}^m\|^2 = \|\boldsymbol{P}_{\perp}\boldsymbol{b}^m\|^2 \tag{5.6}$$

where $\boldsymbol{P}_{\|}$ is the projector onto the subspace spanned by the columns of $\boldsymbol{A}$ and $\boldsymbol{P}_{\perp}$ is its orthogonal projector. When the current dipole positions are unknown and are sought by means of an iterative procedure, the current dipole moments and the residual at each step of the iteration may be found by means of formulae (5.4) and (5.6). The iterative search for the minimization of (5.3) is a computationally demanding problem because of the large number of nonlinear parameters, because it is difficult to provide a good first guess and, finally, because the algorithm may become trapped in a local minimum. An algorithm called MUSIC (multiple signal classification) that simplifies the search for multiple sources was proposed by Mosher *et al* (1992).

The first issue to address in a multiple-source inverse solution is the number of sources, which is fixed in the formalism of (5.2). This may be done by inspecting the matrix $\boldsymbol{b}^m$ of measured magnetic field values. Munck (1990) found a lower bound for the residual R, which is independent of the head model used for theoretical field calculation:

$$R \geqslant \sum_{j=r+1}^{s} \beta_j^2 \tag{5.7}$$

where r is the rank of the matrix $\boldsymbol{b}$, s is the rank of the matrix $\boldsymbol{b}^m$ and the β_j are the singular values of the matrix $\boldsymbol{b}^m$. Since the rank of the matrix $\boldsymbol{b}$ is not larger than the number N of independent current dipole waveforms in $\boldsymbol{q}$,

$$R \geqslant \sum_{j=N+1}^{s} \beta_j^2. \tag{5.8}$$

To check whether the hypothetical number of dipoles is adequate to fit the data, one may calculate the expression on the right-hand side of (5.6) and compare it with the estimated noise of the data. If it is larger, this means that the residual cannot be explained entirely by the noise, and an additional independent current dipole component must be added to the model. This reasoning however tells us only the total number of independent current dipole components; it does not tell us the total number of current dipoles since those with fixed direction have one independent component while those with variable direction have two. We shall assume here that the current dipoles all have variable direction, so that the number of current dipoles is $N/2$.

The idea of the MUSIC algorithm is, once the number of current dipoles is decided, to find the best projector $\boldsymbol{P}_{\perp}$ that minimizes (5.6) irrespective of matrix $\boldsymbol{A}$. Then find the matrix $\boldsymbol{A}$ such that $\boldsymbol{I} - \boldsymbol{A}\boldsymbol{A}^+$ best approximates $\boldsymbol{P}_{\perp}$. Finally, find the current dipole moment time courses by means of (5.4).

The best projector $\boldsymbol{P}_{\perp}$may be found by singular value decomposition of the data matrix $\boldsymbol{b}^m$, while the matrix $\boldsymbol{A}$ is ideally orthogonal to $\boldsymbol{P}_{\perp}$ so that $\boldsymbol{A}$ may be found by minimizing

$$R' = \|\boldsymbol{A}^t\boldsymbol{P}_{\perp}\|^2. \tag{5.9}$$

By decomposing $\boldsymbol{A}$ into $N/2$ $M \times 2$ submatrices $\boldsymbol{A}_j$, one for each current dipole in the model, it may be shown that

$$R' = \sum_{j=1}^{N/2} \text{Tr}(\boldsymbol{A}_j^t\boldsymbol{P}_{\perp}\boldsymbol{A}_j) = \sum_{j=1}^{N/2} R'_j. \tag{5.10}$$

The minimum of R' corresponds to the simultaneous minima of all the R'_j. Since the latter depend only on one current dipole location, all these minima may be found by one scan of the whole brain volume.

5.3. Linear estimation

Another possibility to reconstruct neural activity in the case of multiple sources is to use as the source model a large number of fixed ECDs located at known positions—i.e. a current dipole field. The ECDs in this case usually have a fixed direction, and are distributed in the brain model in such a way that they cover the areas where activity is expected. For example, in a realistic brain model for linear source estimation, the current dipole field covered the whole cortex, and the single current dipoles were orthogonal to the cortex surface at their location (Babiloni *et al* 2001). It is also possible to arrange three current dipoles at the same location with moments pointing in three orthogonal directions. In general, the theoretical field generated by the dipole field may be expressed as in (5.2). In contrast with the multiple dipole model, the locations of the current dipoles are known so the matrix $\boldsymbol{A}$ is also known, and (5.2) is in this case a linear system of equations. The solution we seek is an array of current dipole amplitudes at each time-slice of the data. The coverage of a reasonable cortical area, or brain volume, requires a large number of current dipoles, much larger than the number of magnetic field measurements, so that the system is highly underdetermined. Usually, the current dipole field samples closely the investigated area or volume. As a consequence, columns of $\boldsymbol{A}$ corresponding to neighbouring current dipoles are almost linearly dependent on each other. The matrix $\boldsymbol{A}^t\boldsymbol{A}$ is close to singular, and the solution (5.4) either is not unique or has large fluctuations depending on the noise in $\boldsymbol{b}^m$. In this case the variability of the solution is constrained by a procedure known as regularization (Tikhonov and Arsenin 1977), thereby increasing its stability. The solution $\boldsymbol{q}$ is found by minimizing the following quantity:

$$\Psi(q) = \|\boldsymbol{D}(\boldsymbol{b}^m - \boldsymbol{A}\boldsymbol{q})\|^2 + \lambda^2\|\boldsymbol{C}\boldsymbol{q}\|^2 \tag{5.11}$$

where $\boldsymbol{C}$ and $\boldsymbol{D}$ are two conditioning matrices that allow the application of different weights to current dipoles and to sensors, respectively. The matrix $\boldsymbol{D}$ usually takes into account the noise statistics in the data, and a typical choice is to derive it from the covariance matrix $\boldsymbol{S}$ according to

$$\boldsymbol{D}^t\boldsymbol{D} = \boldsymbol{S}^{-1}. \tag{5.12}$$

The matrix $\boldsymbol{D}$ is also useful to combine EEG with MEG data, in order to take into account scaling factors between the two types of datum (Babiloni *et al* 2001). The matrix $\boldsymbol{C}$ describes the kind of regularization that is applied to the solution. For example if $\boldsymbol{C}$ is the identity matrix, then the solution is a minimum-norm solution. This type of solution favours shallower current dipoles at the expense of deeper current dipoles since the former generate stronger fields with the same current dipole amplitude. To compensate for this tendency, one may use as the matrix $\boldsymbol{C}$ a diagonal matrix $\boldsymbol{W}$, the diagonal elements of which are the norms of the corresponding columns of matrix $\boldsymbol{A}$:

$$W_{ii} = \|\boldsymbol{A}_{\cdot i}\|. \tag{5.13}$$

In the implementation known as LORETA (low-resolution electromagnetic tomography, Pascual-Marqui *et al* 1995) $\boldsymbol{C}$ is the product of the above matrix $\boldsymbol{W}$ with the discrete Laplacian operator $\boldsymbol{B}$:

$$\boldsymbol{C} = \boldsymbol{B}\boldsymbol{W}. \tag{5.14}$$

This choice for $\boldsymbol{C}$ has the effect of maximizing the smoothness of the solution. This choice was made on physiological grounds to take into account the synchronous activity of neighbouring neurons.

Matrix $\boldsymbol{C}$ may also be used to take into account *a priori* information on the source, either coming from anatomic–physiological knowledge, or obtained by means of other imaging techniques such as functional magnetic resonance imaging (fMRI). For example, in order to constrain the solution to have larger amplitudes in the proximity of observed fMRI activations, the following diagonal matrix $\boldsymbol{C}$ was used (Cincotti *et al* 2001):

$$C_{ii} = W_{ii}/g(a_i) \tag{5.15}$$

where g is an increasing function of fMRI signal intensity a_i in the neighbourhood of the ith current dipole.

Finally, λ in formula (5.11) is a regularization parameter that permits one to tune the weight of the regularization constraint in the minimization of $\Psi(\boldsymbol{q})$. For $\lambda = 0$, no constraint is imposed on the solution. Optimal regularization may be obtained by selecting the value of λ according to the L-curve approach (Hansen 1992). The L-curve plots the residual norm—the first term in the right-hand side of (5.11)—versus the regularized solution norm—the second term—at different λ-values. The inspection of the L-curve allows the selection of a λ-value which is a compromise between the minimization of the above two quantities. The use of the L-curve can be traced back to the work of Miller (1970) and Lawson and Hanson (1974).

5.4. Lead field theory

From the theory developed in sections 3 and 4, and from the observation closing the introduction of section 5, it is readily observed that the output of a channel of measurement is a linear functional of the impressed current density function $\boldsymbol{J}^i$. Thus, if b_j^m is the output of the jth channel, we may write

$$b_j^m = \int \boldsymbol{L}_j(\boldsymbol{x}) \cdot \boldsymbol{J}^i(\boldsymbol{x})\, \mathrm{d}v \tag{5.16}$$

where the integral is extended to the volume where the function $\boldsymbol{J}^i$ is defined. Referring to the notations of (3.36), we shall call this volume V_0 but it may as well be any subset of it. The vector function $\boldsymbol{L}_j$ is called the *lead field* of the jth channel. The meaning of $\boldsymbol{L}_j(\boldsymbol{x})$ may be understood by observing that if we place in turn three unit current dipoles at $\boldsymbol{x}$, pointing along the three axes of the coordinate system, the corresponding outputs of the jth channel are the three components of $\boldsymbol{L}_j(\boldsymbol{x})$. This also represents a means of calculating $\boldsymbol{L}_j(\boldsymbol{x})$ explicitly when the forward problem for the particular instrument configuration and volume conductor model is solved.

Let us now consider the vector space $\mathcal{F}$ of all the vector functions defined in V_0. We may define an inner product in $\mathcal{F}$, according to

$$(\boldsymbol{U}, \boldsymbol{V}) = \int \boldsymbol{U}(\boldsymbol{x}) \cdot \boldsymbol{V}(\boldsymbol{x})\, \mathrm{d}v. \tag{5.17}$$

Then, formula (5.16) states that the output of the jth channel is the inner product of the primary current density and the lead field of that channel. It follows that (1) only primary current densities that have a nonvanishing projection onto $\mathcal{G} = LS\{\boldsymbol{L}_1, \ldots, \boldsymbol{L}_M\}$, the vector subspace spanned by the lead fields, will yield a nonvanishing set of channel outputs; (2) from our set of channel outputs $\{b_j^m\}$ we may only reconstruct a current density function belonging to $\mathcal{G}$. In other words the component of $\boldsymbol{J}^i$ orthogonal to $\mathcal{G}$ is magnetically silent for our instrument and may not be retrieved from magnetic field measurements. This result suggests a point of

view regarding the restriction of possible solutions to the inverse problem that consists of seeking a solution in the subspace $\mathcal{G}$. Such a solution $\boldsymbol{J}^s$ will therefore be a linear combination of the lead fields:

$$\boldsymbol{J}^s = \sum_{j=1}^{M} \alpha_j \boldsymbol{L}_j. \tag{5.18}$$

Such a solution is called a minimum norm estimate (Hämäläinen and Ilmoniemi 1984, 1994) because it is the current density function with the smallest norm—as derived from (5.17)—that explains the measured signals.

If $\boldsymbol{J}^s$ is the projection of $\boldsymbol{J}^i$ onto $\mathcal{G}$, then $(\boldsymbol{L}_j, \boldsymbol{J}^s) = (\boldsymbol{L}_j, \boldsymbol{J}^i) = b_j^m$. The coefficients α_j are thus the solution of a linear system of equations:

$$\boldsymbol{\Lambda}\underline{\alpha} = \underline{b}^m \tag{5.19}$$

$\boldsymbol{\Lambda}$ is an $M \times M$ matrix the elements of which are the inner products of the lead fields:

$$\Lambda_{jk} = (\boldsymbol{L}_j, \boldsymbol{L}_k). \tag{5.20}$$

The lead fields are in principle linearly independent, and the matrix $\boldsymbol{\Lambda}$ is therefore invertible. However, neighbouring channels may have similar lead fields so that some columns of $\boldsymbol{\Lambda}$ may be close to linearly dependent, and the matrix close to singular. In this case $\boldsymbol{\Lambda}$ has some very small eigenvalues, and direct inversion of (5.19) may lead to large errors in $\underline{\alpha}$. A method to overcome this difficulty is to apply a truncated singular value decomposition:

$$\boldsymbol{\Lambda} = \boldsymbol{V}\boldsymbol{\Sigma}\boldsymbol{V}^t \tag{5.21}$$

where $\boldsymbol{V}$ is an orthogonal matrix and $\boldsymbol{\Sigma}$ is a diagonal matrix, the elements of which are the eigenvalues σ_j of $\boldsymbol{\Lambda}$ arranged in decreasing order. The truncation consists in the suppression (replacing with zero) of the smallest eigenvalues, and of the corresponding subspaces of $\mathcal{G}$, and then taking the inverse. We finally obtain the solution:

$$\underline{\alpha}' = \boldsymbol{\Lambda}'^{-1}\underline{b}^m \tag{5.22}$$

where $\boldsymbol{\Lambda}'^{-1} = \boldsymbol{V}\boldsymbol{\Sigma}'^{-1}\boldsymbol{V}^t$ with $\boldsymbol{\Sigma}'^{-1} = \mathrm{diag}(\sigma_1^{-1}, \ldots, \sigma_k^{-1}, 0, \ldots, 0)$. The cutoff index k is selected so that the residuals $\underline{b}^m - \underline{b}'$ between the measured signals $\underline{b}^m$ and the reconstructed signals $\underline{b}' = \boldsymbol{\Lambda}\underline{\alpha}'$ are of the same order of magnitude as the noise in the signals.

6. Instrumentation for magnetoencephalography

The challenge for biomagnetic instrumentation is the detection of extremely weak magnetic signals (1 fT to 100 pT) in the presence of a very noisy background ($\sim$10 μT and above). Properly designed instrumentation must therefore be endowed with sensitive magnetic field detectors, and sophisticated noise cancellation techniques. Another aspect is represented by the suitability for clinical application of the technique, where the necessity of measuring the magnetic field over the entire area of the head is mandatory for a practical clinical use of neuromagnetism.

In the last 8–10 years several large multichannel sensors have been developed, and today about 100 institutions worldwide currently use neuromagnetic systems. Most of the systems used by the experimenters and/or clinicians are produced and sold by two companies: 4-D Neuroimaging (9727 Pacific Heights Boulevard, San Diego, CA 92121-3719, USA—www.4dneuroimaging.com), a new company resulting from the acquisition of Neuromag Ltd by the former Biomagnetic Technologies Inc, and CTF Systems Inc. (15-1750 McLean Avenue, Port Coquitlam, B.C., Canada V3C 1M9—www.ctf.com); but other companies or single institutions have also developed their own devices.

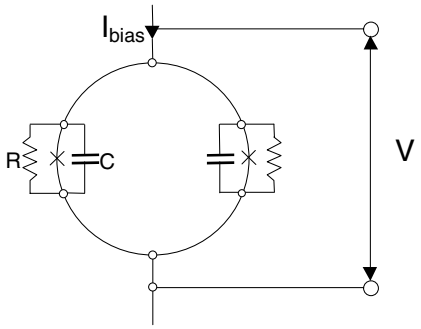

Figure 6. Schematic diagram of a dc SQUID. The Josephson junction is denoted by a cross. The capacitor is due to the stray capacity of the junction, while the resistor is added to remove the hysteretic behaviour of the junction itself.

There are several published papers covering different aspects of biomagnetic instrumentation. A complete and detailed reference on many issues related to biomagnetic instrumentation may be found in a NATO–ASI book edited by Weinstock (1996). Other details concerning biomagnetic instrumentation may be found in a recent review by Pizzella and co-workers (2001) or in the proceedings of the *Applied Superconductivity Conferences* (see for instance the review by Wikswo (1995)). However, the best up-to-date documentation for biomagnetic instrumentation is the latest *BIOMAG* conference proceedings (Yoshimoto *et al* 1999, Nenonen *et al* 2000).

6.1. The SQUID

SQUID devices are used in all neuromagnetic systems. Their principles of operation rely on two phenomena observed in superconductors: the quantization of the magnetic flux through a loop, that must be an integer multiple of $\Phi_0 = h/2e = 2.07 \times 10^{-15}$ Wb; and the Josephson effect. Indeed, the first SQUIDs were built after the prediction by Josephson (1962) that in superconductors Cooper pairs (pairs of electrons which are the charge carriers of the supercurrent) may tunnel across an insulating barrier. This phenomenon is named the Josephson effect, and the barrier is named the Josephson junction. The dc SQUID is realized by combining two junctions in parallel (see figure 6), and its principle of operation is based on the interference of the phase of the wavefunction describing the condition of a Cooper pair across each junction. This interference changes according to the magnetic flux coupled to the SQUID ring and, as an overall result, this modulates the voltage across the device. This device is called a dc SQUID since a steady bias current I_{bias} can be used to operate it. The development of the dc SQUID is one of the most remarkable applications of superconductivity: in fact the dc SQUID is the most sensitive magnetometer currently available in the dc–MHz range, and using a dc SQUID it is possible to build the fastest amplifiers with the lowest noise (close to the quantum limit). (For a review on dc SQUIDs see for example the work of Clarke (1996).)

The first SQUID used for neuromagnetic measurements, designed by Zimmerman in the mid-1960s (Zimmerman and Silver 1966), was actually a different kind of SQUID, the rf SQUID, the name of which is due to the fact that this type of SQUID must be driven by an ac current. The rf SQUID consists of a superconducting loop interrupted by a single Josephson junction, coupled to a resonant tank circuit that is tuned to an externally supplied sinusoidal biasing current in the radio-frequency range (typically tens or hundreds of megahertz). The rf SQUID actually operates according to a different physical phenomenon: it is practically a parametric amplifier (with device noise inversely proportional to the driving frequency), and no superconducting interference takes place. The requirement for only one junction is the reason why this device was first used. The performance of this type of SQUID are inferior

to those of the dc SQUID. Today the thin-film microfabrication technology of niobium (the superconducting element used for the fabrication of these devices) allows us to build two identical and stable high-quality Josephson junctions, which are needed in a dc SQUID, and rf SQUIDS are no longer used in multichannel neuromagnetic systems. An important exception is the case of high-temperature superconductors (HTSs). The HTS junction technology is still not able to realize pairs of identical and stable junctions, at least not in a reproducible way, and therefore HTS rf SQUIDs are used for the fabrication of small multichannel devices.

In the frequency range of biomagnetic applications, the sensitivity of the instrumentation is limited by two types of noise component: the Nyquist noise, which has a uniform spectral density, and a second noise component which increases at low frequency, the so called '$1/f$ noise'. The onset of the '$1/f$' noise, i.e. the frequency below which this component becomes dominant, varies depending on the SQUID technology and the operating conditions. This 'corner frequency' is typically in the region of 1 Hz.

The present technology allows one to build LTS dc SQUIDs with a magnetic flux sensitivity $S_\Phi^{1/2} \leqslant 1 \times 10^{-6}\Phi_0\ \mathrm{Hz}^{-1/2}$. The best dc SQUID ever fabricated to be used as a magnetic field detector featured a flux sensitivity noise of $S_\Phi^{1/2} = 1.25 \times 10^{-7}\Phi_0\ \mathrm{Hz}^{-1/2}$ at 4.2 K (Carelli *et al* 1998), but its design did not allow a large yield and this low noise figure critically depended on the bias parameters.

A more useful noise figure is the SQUID magnetic field sensitivity $S_B^{1/2}(f)$, which includes the effect of the pick-up coil: $S_B^{1/2}(f) = S_\Phi^{1/2}(f)/A_{\mathrm{eff}}$, where A_{eff} is the effective area of the pick-up coil. By enlarging the effective area of the pick-up coil it is possible to reach a high field sensitivity; however, this introduces some limitation in the overall spatial resolution of the multichannel system. Neuromagnetic measurements require a detection device with a field sensitivity $S_B^{1/2}(f)$ of about 5 fT $\mathrm{Hz}^{-1/2}$ in the white region and less than 20 fT $\mathrm{Hz}^{-1/2}$ at 1 Hz.

6.2. The single-channel biomagnetic system

To describe a typical neuromagnetic system it is useful to consider a simple system measuring the magnetic field value at one point in space. Actually, since the magnetic field is a vector, three orthogonal components should be measured using three different sensors, but most of the neuromagnetic sensors actually measure only one component of the magnetic field. In the following we shall refer to 'the magnetic field sensed by a detection coil at one point in space', although it really senses only one component of the magnetic field at that point.

A simplified block diagram for this simple sensor is shown in figure 7; the actual detectors are made by simply increasing the numbers of sensing units. The basic neuromagnetic system consists of (i) the SQUID, (ii) the detection coil, (iii) the cryostat, (iv) the room-temperature readout electronics and (v) the shielded room.

6.2.1. The detection coil. In practice, it is not convenient to use the SQUID loop to directly sense the field, mainly because the SQUID inductance must be small in order to minimize the noise of the detector. Additionally, it is convenient to use a separate detection coil to sense the external magnetic field, because in this way it is possible to change the field spatial sensitivity of the device without affecting the SQUID design. The magnetic flux sensed by the detection coil is transferred to the SQUID through an input coil which is often built directly onto the SQUID chip (see figure 8). It is worth noting that the entire flux transformer—detection coil and input coil—is a superconducting loop. Thus, the external magnetic field induces a current in this loop which is proportional to the field itself.

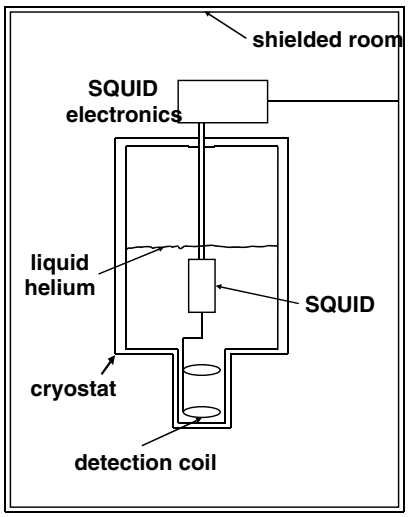

Figure 7. Schematic diagram of a single-channel neuromagnetic system.

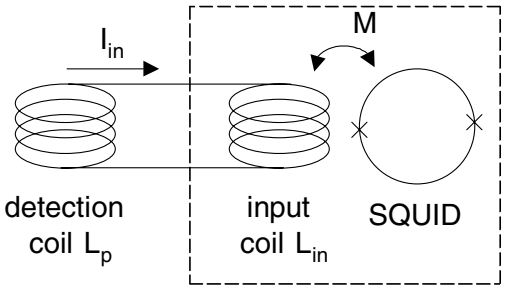

Figure 8. Schematic diagram of a SQUID loop with the flux transformer. The dashed box is integrated on a planar chip. The magnetic field is sensed only by the detection coil, while the SQUID loop is coupled only to the input coil.

The simplest detection coil, namely a magnetometer, is made by a single turn (or few turns) of superconducting wire. If the magnetic field is constant over the coil area, the current flowing in the loop is simply proportional to the field intensity. The important advantage of this simple type of detection coil is that it is easy to integrate within the SQUID chip, thus simplifying the construction of complex multichannel biomagnetic systems. The multiturn coil is the best type of detection coil from the sensitivity point of view. Specific geometries for the detection coil may reduce conveniently the sensitivity to noise sources, with little loss of sensitivity for the biomagnetic sources of interest. The most used detection coil of this type is the first-order gradiometer, which is made by adding two magnetometer coils wound in an opposite sense. These coils may be displaced along their common axis (producing an axial gradiometer) or in their common plane (producing a planar gradiometer). Similarly, a second-order axial gradiometer may be used. This device couples two first-order gradiometers end to end, yielding a detector which is insensitive to spatially uniform fields and linear gradients. This type of coil system was very popular in the early days of biomagnetism when single-channel or small multichannel systems were built for operation in unshielded environments.

To best couple the SQUID to the detection coil some simple rules must be observed. The flux Φ_s coupled to the SQUID ring is

$$\Phi_s = MI_{in} = M\Phi_p/(L_p + L_{in})$$

where M is the mutual inductance between the input coil and the SQUID loop and Φ_p is the magnetic flux coupled to the detection coil. The ratio between Φ_s and Φ_p is

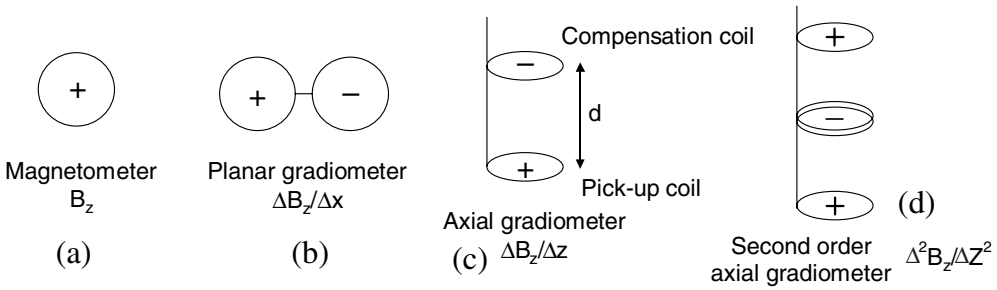

Figure 9. Different types of detection coil.

$$\Phi_s/\Phi_p = M/(L_p + L_{in}).$$

To maximize this value (once the SQUID parameters are fixed) L_p must be chosen to satisfy the matching condition: $L_p = L_{in}$. If this condition is not satisfied the energy sensed by the detection coil is not optimally transferred to the SQUID; however, the energy transfer as a function of L_p/L_{in} is quite smooth and a mismatch of the inductance of a factor of four causes a reduction of the sensed signal of only about 20% (Carelli and Pizzella 1992).

Figure 9 illustrates some of the most widely used detection coils. The characteristics of these detection coils, especially with respect to their noise reduction properties, will be discussed in section 6.4. A complete dissertation on the performance of the different types of detection coil may be found in Vrba (1996).

6.2.2. The cryostat. Unfortunately, superconductivity shows up only at a very low temperature, and therefore the SQUID detector must be cooled for proper operation. All currently used large neuromagnetic systems use LTS materials, hence liquid helium is used as cooling fluid to reach a temperature of 4.2 K. The cryostat (dewar) enclosing the probe is a critical part of the instrument and must satisfy severe requirements: (i) the material used for fabrication must be nonmagnetic; (ii) the magnetic noise must be less than the noise of the sensors and (iii) the distance of the detection coils from the head of the subject must be as small as possible.

Usually fibreglass is used as a material to build the dewar, since it has optimal magnetic properties. However, its use poses some problems in the mechanical stability of the dewar, especially in the region where the detection coils are hosted. To guarantee the safety of the subject, thick fibreglass layers are used, especially in flat-bottomed systems, but this causes the detection coils to be far from the subject. Moreover fibreglass does not provide any shield against radiation, and therefore, many (50–100) layers of mylar must be wrapped around the inner portion of the dewar for radiation shielding. These shields increase the magnetic noise of the dewar, since eddy currents are allowed to flow on the aluminated side of the mylar (Hämäläinen *et al* 1993), and a compromise must be made to obtain the best overall performance. Typical biomagnetic dewars exhibit noise below 5 fT $Hz^{-1/2}$, that, however, may be the limiting noise factor of the sensor.

Finally, when designing clinical systems, it is important to consider practical issues for system operation and maintenance. For instance, the helium reservoir should be large enough to ensure several days between helium refills, yet without increasing by too much the external dimensions and weight of the dewar. Typical whole-head neuromagnetic dewars have a helium capacity of about 60–80 l with a helium refill interval of 5–7 d.

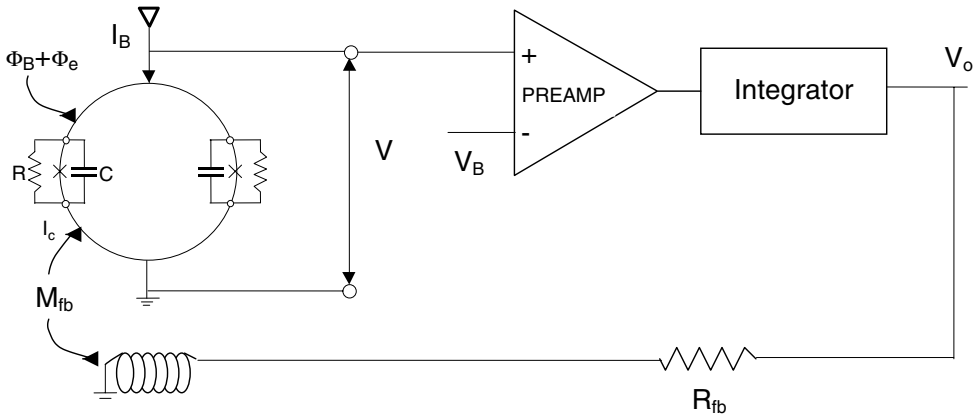

Figure 10. Simplified scheme of the FLL configuration. I_B, Φ_B, V_B determine the working point of the SQUID; the feedback inductance is coupled negatively to the SQUID, so that V_0 is linearly related to the external applied flux Φ_e.

6.2.3. The room-temperature readout electronics. The SQUID readout electronics varies according to different SQUID features: a more complex scheme exhibits better performance in terms of noise, dynamics and slew rate, but has more integration problems; a simpler design is easily integrated but the above features are not as good. The choice of the specific design is also related to the specific SQUID sensor. SQUIDs with high noise in the low-frequency band (e.g. HTS SQUIDs) must use suitable electronics to minimize this noise. Indeed, the use of a large number of SQUIDs in neuromagnetic systems requires easily operated, simple and compact size room-temperature electronics.

A common feature to all SQUID electronics is the flux-locked loop (FLL) configuration. As already mentioned, the SQUID behaves as a magnetic flux-to-voltage converter, with a nonlinear, periodic response to an externally applied flux. In order to make the sensor output a linear function of the applied flux, the SQUID must be operated in an FLL configuration, where the working point of the SQUID, identified by a bias flux Φ_B and a bias voltage V_B, is maintained fixed by a negative feedback. A schematic diagram of the FLL circuit is shown in figure 10: a preamplifier and an integrator processing the SQUID output are used; the output voltage is converted into a zeroing flux by means of a resistor R_{fb} and a coil coupled to the SQUID with mutual inductance M_{fb}, both composing a negative feedback loop. The output voltage V_o is directly proportional to the external applied flux Φ_e by a constant factor R_{fb}/M_{fb}.

Practical schemes must take into account the impedance mismatch between the SQUID and the preamplifier. There are two simple ways of doing so: a flux modulation technique may be used, or positive feedback may be applied. In the first case, a modulating flux is applied to the SQUID, the output of which is amplified and processed by means of a lock-in detector, utilizing the flux modulation frequency f_{mod} as the reference frequency. The preamplifier noise contribution is strongly reduced by coupling the low impedance of the SQUID to the high input impedance of the preamplifier through a cooled matched transformer. Additionally, the low-frequency noise determined by the bias current fluctuations in the SQUID and by the preamplifier does not contribute to the overall system noise. On the other hand, the flux modulation technique has two main drawbacks: the complexity of the electronics is high; the channel interference may be a problem, and careful shielding of the wires and electronics is mandatory. In the second case the SQUID is coupled directly to the room-temperature amplifier and no flux modulation is used. The preamplifier contribution to the overall sensor noise is

reduced by increasing the SQUID sensitivity $V_\Phi = \partial V/\partial\Phi$, thus increasing the voltage output of the SQUID. With this method, only four wires are needed to connect the SQUID to room-temperature electronics, without any need for shielding to prevent crosstalk between adjacent channels. Additional details on the different types of SQUID electronics may be found in the work of Drung (1996).

6.3. Magnetic noise rejection

To properly perform biomagnetic measurements the instrumentation must have not only a very high sensitivity, but also the ability to reject environmental noise. There are three possible ways to handle environmental noise: (i) using detection coils designed with a specific geometry able to discriminate between signals from close sources (i.e. sources of interest) and signals from remote sources (i.e. disturbances); (ii) using separate detectors to sense the environmental noise and a high-performance electronic subsystem (real-time hardware and software) for subtraction of the noise from the sensors and (iii) using magnetically shielded rooms to reduce the environmental noise to an acceptable level.

Of course, these three approaches can be combined to achieve the best price-to-performance ratio. A common solution is a combination of first-order gradiometric pickup coils together with moderate passive shielding like a double-layer shielded room.

6.3.1. Use of detection coils. A magnetometer responds to the applied field regardless of the distance to the source but other detection coils can conveniently reduce the sensitivity to far sources. A first-order gradiometer is insensitive to spatially uniform fields, whereas a second-order gradiometer is insensitive to both uniform fields and gradients. By using these more complex geometries a 'noise' field produced by far sources (relative to the distance b between the subcoils, the so-called baseline of the gradiometer), can be substantially cancelled, whereas a high sensitivity is still available for sources that are located at a distance smaller than the baseline. The (small) penalty paid for such ambient noise reduction is a reduction in overall sensitivity, since the signal energy is shared among the subcoils of the gradiometer.

To quantify this fact let us consider a dipolar source located on the axis of a first-order axial gradiometer (figure 9(c)) at a distance r from the bottom coil. The total flux sensed by the detection coil is the difference between the flux sensed by the pick-up coil and the flux sensed by the compensation coil:

$$\Phi_B = C\left(\frac{1}{r^2} - \frac{1}{(r+b)^2}\right) = \frac{C}{r^2}\left(1 - \frac{1}{(1+b/r)^2}\right)$$

where C is a constant depending on the source intensity, and b is the baseline of the gradiometer. In the two limits of a near and far source

$$\Phi_B \approx C/r^2 \qquad \text{for} \quad b \gg r$$
$$\Phi_B \approx C/r \qquad \text{for} \quad b \ll r.$$

The gradiometer acts like a magnetometer ($1/r^2$ law), if the source is closer to the pick-up coil than the baseline of the device. On the other hand, far-away sources are sensed with lower sensitivity, since the flux is proportional to $1/r^3$. Similarly a $1/r^4$ law is obtained for distant sources measured with a second-order gradiometer (figure 8(d)).

6.3.2. Electronic noise subtraction. A different approach to noise reduction consists in the use of simple, integrated SQUID magnetometers plus additional reference sensors displaced at

a convenient distance from the main array to sense the ambient noise. After the measurement of the magnetic field has been carried out with the standard SQUID electronics, the noise may be subtracted on line in a DSP, as well as off line during signal processing by performing a suitable linear combination of the measured field values.

There are many advantages to this approach: a magnetometer is much easier to fabricate since the loop may be integrated directly onto the SQUID chip, and this is a crucial point particularly when building HTS sensors. It is possible to reconfigure the sensing array to simulate different kinds of detection coil, e.g. first-order axial or planar gradiometers. Additionally it is possible to minimize the overall field sensed by each sensor before the measurement, thus forming an adaptive magnetometer. This approach guarantees better performance with respect to the previous one, at least if the noise sources are stationary (Vrba 1996). If the source characteristics do vary in time, the mean performance of the adaptive noise cancellation is inferior to that of the software gradiometers with fixed compensation coefficients.

The main disadvantage in using electronic noise subtraction is that when the SQUID is coupled to a magnetometer, the electronics must have a larger dynamic range and a higher slew rate to keep it locked, since it must sense larger field variations. Moreover more SQUIDs are needed, since both noise field and noise gradient values are used in the process of noise subtraction. Lastly the use of a good-quality shielded room is mandatory.

6.3.3. Shielded rooms. In the frequency range of interest for biomagnetic measurements, the problem of shielding can be analysed in a quasistatic approximation in terms of a magnetic circuit. The soft magnetic material (iron alloys with $\mu > 10^4$) acts as a 'high-conductivity' conductor for the magnetic flux, as compared with the conductivity of the space enclosed in the shielded room. In this way a large part of the flux is concentrated in the walls and only a small part can enter the room. The total shielding factor is related to the total amount of the soft magnetic material used, and to the number and mutual distance of the layers in which the material is shaped.

The shielding effect relies also on eddy current shielding. The efficiency of the shield depends on the wall thickness, on the conductivity of the materials and on the frequency of the external magnetic field: in the range of power line frequency (50 or 60 Hz), an aluminum wall thickness of 50 mm is required to obtain a shielding of 60 dB. Additionally, the high-conductivity layer provides radio-frequency shielding (frequency above $\sim$100 kHz). Although there is no neuromagnetic field at such high frequencies, the presence of radio frequency may spoil SQUID noise performance, and is therefore important to keep the superconducting neuromagnetic sensor radio-frequency-free.

To improve the shielding factor, especially at low frequency, it is possible to use an additional 'active' shield using large Helmholtz-like coils wound around the external walls of the room (ter Brake *et al* 1993). This value is then minimized by feeding the appropriate current in the external coils. Usually this shielding is effective at frequencies lower than 1–2 Hz, unless separate coils for low- and high-frequency compensation are provided (Pasquarelli *et al* 1999).

As an example of a typical (2 + 1)-layer (two layers of high-μ material plus one aluminium layer) shielded room without active compensation, we consider the room model AK3b by Vacuumschmelze Gmbh (Grüner Weg 37, D-63450 Hanau, Germany—www.vacuumschmelze.de). Typical shielding factors obtained for this room are about 58 dB at 1 Hz, and 100 dB at 50 Hz.

The best shielding values ever measured are those of a massive shielded room built recently by Vacuumschmelze and installed at the Physikalisch-Technischen Bundesanstalt (PTB) in Berlin (Bork *et al* 2001) with one layer of aluminium and seven layers of high-μ material

(outer dimensions $15 \times 15 \times 15$ m^3, inner dimensions $2.9 \times 2.9 \times 2.9$ m^3): its passive shielding factors are 100 dB at 0.05 Hz and 126 dB at 1 Hz. With active shielding, impressive shielding factors of 130 and 142 dB respectively were achieved (Nowak, personal comunication).

6.4. Multichannel neuromagnetic systems

Multichannel systems for MEG measurements consist of a large number of sensing channels covering the whole head, allowing the simultaneous recording of the magnetic field at many points over the scalp in a single measurement. Currently operating neuromagnetometers are based on stable and robust LTS dc SQUIDs and feature a high magnetic field sensitivity, with $S_B^{1/2} < 10$ fT Hz$^{-1/2}$ in the white-noise region of the spectrum. The sensing elements are dc SQUID magnetometers or gradiometric flux transformers, planar or axial, with pick-up coil areas ranging from 1 to 4 cm^2. In the large majority of cases only one component of the magnetic field is detected (e.g. B_r), while only a few recent experimental multichannel MEG systems use triplets of orthogonal pick-up coils to detect all three components of the field. The pick-up coils are placed at the bottom of a helmet-shaped dewar, generally fitting the adult head. The dewar itself may be tilted to better accommodate the subject, and the tilt may be large enough to allow measurements in both the seated and the supine position. EEG recordings simultaneous with magnetic signals are always provided. The A/D conversion unit samples the data (both magnetic and electric) at a fixed or selectable sampling frequency. The number of bits of the A/D conversion data determines the overall dynamic range of the system, and is usually between 16 and 32. A digital data preprocessing unit is usually provided for signal conditioning, in order to minimize interchannel delay and performance mismatch.

As an example of a multichannel neuromagnetometer, the prototype whole-head MEG system installed at the University of Chieti (Della Penna *et al* 2000) is shown in figure 11. This sensor has been developed within the framework of an international co-operation among research institutions: ITAB—University of Chieti, Institute of Cybernetics—CNR, Naples, Italy, ZIBMT—University of Ulm, Germany, and a company, ATB—Chieti, Italy.

This system consists of 165 dc SQUID integrated square magnetometers, with a pick-up coil area of 91 mm^2 size. The sensor layout is the following: 153 channels are placed, with an inter-sensor spacing of about 3.2 cm, on a helmet shaped surface; 12 channels are arranged in four orthogonal triplets at a distance of 7 cm from the measurement surface and are used as references for the software rejection of the background noise. The sensor array is placed inside a dewar ($S_B^{1/2} < 3$ fT Hz$^{-1/2}$), containing about 83 l of liquid helium and requiring one refilling per week; the distance between the measurement surface and room-temperature space is about 1.8 cm.

The SQUID electronics is based on FLL direct readout and placed, on the top of the dewar, on a circular motherboard, which also contains the control logic unit. The system is located inside a good-quality shielded room, made of one external aluminium layer, 12.7 mm in thickness, for high-frequency shielding and 4 internal layers of high-magnetic-permeability material, 1.57 mm in thickness. The shielding factor is about 49 dB at 0.01 Hz and 110 dB above 40 Hz.

7. Data acquisition and analysis

All biomagnetic measurements are performed using computerized data acquisition systems, therefore signal conditioning is required to best match the amplitude and bandwidth of the signal with the dynamic range, the resolution and the sampling rate of the analogue to digital converter (ADC) in use. Thanks to the advent of digital signal processors (DSPs), the

Figure 11. The 165-channel MEG system installed at ITAB, University of Chieti.

implementation of digital filters with much better performance than their analogue counterparts is now possible at very reasonable prices. Therefore, the use of analogue filters is limited to dc filtering to avoid offset problems and anti-aliasing low-pass filters prior to A/D conversion.

7.1. Analogue signal processing

The requirements for the analogue signal filtering are determined by the ADC. The ADC dynamics, and of course the environmental noise, may force the use of an analogue high-pass filter to avoid signal overflows; the ADC sampling frequency, f_s, sets the analogue low-pass filter.

As for the high-pass filter, usually a first-order filter is employed, with cut-off frequency as low as possible according to the ADC dynamic range. With regard to the low-pass filter, to avoid aliasing it is necessary that the amplitude of the harmonic spectrum at frequencies equal to or above $f_s/2$ is below the sensitivity of the A/D converter. Since it is impossible to design a distortion-free low-pass filter featuring a transfer function with such a steep drop in the forbidden band, it is advisable to use low-pass filters with cutoff frequencies at 1/3–1/4 of the sampling frequency. Usually 48 dB/octave or even 96 dB/octave Butterworth filters are used, and to ensure a linear phase shift in the signal bandwidth the cutoff frequency is usually set at one-third or one-quarter of the sampling frequency.

7.2. Analogue-to-digital conversion

Two main features must be checked when considering analogue-to-digital conversion: A/D converter speed and resolution. A typical sampling frequency for neuromagnetic measurements is 1 kHz, since the signal is limited to the frequency band below a few hundred hertz. Only

in a few cases may the sampling frequency be increased to 4–5 kHz, with a signal bandwidth of 1–2 kHz. Since modern A/D converters are much faster and less expensive than earlier ones, also thanks to the widespread use of CD players, it is now a good choice to perform the A/D conversion by 'oversampling' at a much higher frequency (up to 100 times) than the signal bandwidth, therefore setting less restrictive features on the analogue low-pass filter. For instance, if a 1000 Hz sampling frequency is required, a 64 times oversampling may be used, i.e. the actual sampling frequency of the A/D conversion may be set at 64 kHz. In this way a simple first-order 6 dB/octave analogue filter may be used as an anti-aliasing filter, with low-pass frequency set at $f_s/64$.

Currently operating neuromagnetometers use an A/D resolution of at least 16 bits. This provides a 96 dB dynamic range, which is large enough for many experimental activities. If magnetometers are used and/or magnetic shielding is poor at low frequency, or a true dc bandwidth is required, a higher dynamic range is desirable. For instance the neuromagnetometer developed by CTF (McKay *et al* 1993) is designed to be operated also in an unshielded environment. To achieve the required dynamic range, the ADC is carried out with 32-bit resolution, thus resulting in a dynamic range larger than 190 dB.

7.3. Digital signal processing and data acquisition

Most of the on-line data treatment (e.g. bandpass filters, line-frequency filters) is done after A/D conversion. For instance, for the case of oversampling, data are sampled at a very high frequency and must be downsampled to the desired rate before being written to disk, to avoid disk filling. Downsampling by a factor of n is simply performed by selecting every nth sample, but, to avoid aliasing, the data are digitally low-pass filtered before discarding the unwanted samples.

There are basically two types of digital filter that can used: finite-impulse-response (FIR) or infinite-impulse-response (IIR) filters (Oppenheim and Schafer 1989). FIR filters are easier to implement but on the other hand require a large number of calculations. For instance, a filter with 100 terms (or taps) will take about 100 multiplications and 100 additions for each sample that comes into the filter. If the sampling rate is 64 kHz, then we have to perform 64 million multiplications per second. IIR filters use feedback terms to dramatically decrease the number of terms that must be taken into account. However designing IIR filters is somewhat similar to designing analogue filters: there are a few standard designs that are mostly used, but their performance is tested only on standard data coming into the filter and, even worse, they are potentially unstable. In practice, since digital processing is becoming cheaper and cheaper, most of the digital filters used are FIR filters, since the easy implementation also implies a larger flexibility for the experimenter.

There are additional advantages in the use of DSPs. First, all the filters have an identical behaviour across different channels, and there are no thermal drifts, aging or noise pickup. Additionally the use of DSPs makes it possible also to build 'virtual sensors' or to perform electronic noise subtraction as described in section 6.4.2 and, today, a modern neuromagnetic system cannot disregard a heavy use of these devices. Last, the on-line data handling makes it possible to monitor the signals and to perform some simple but useful data analysis, such as averaging, in order to check the correctness of the incoming data. Modern multichannel neuromagnetic instruments produce large numbers of data and it is therefore impossible to visually check for every possible overflow or spike on the signal. As a last step, data are finally written on disk for off-line analysis; this was an issue few years ago, but currently available hard disks are able to sustain the required data transfer rate.

7.4. Data analysis

The success of a practical biomagnetic measurement is related to the software available for data analysis. Indeed, the success of the neuromagnetic technique in the clinical environment depends strongly on the whole process of data analysis, which must provide results within a short period of time, including user interface issues, to ensure user-friendly operation. The ultimate goal of data analysis is the determination of the current density inside the brain of the examined subject. This current density is afterwards related to the specific neural activity.

As a general rule, data analysis may be divided into a two-step process: first, the magnetic field values recorded from all sensors are 'de-noised', that is sensor noise and magnetic signals generated by unwanted sources are eliminated to the greatest possible extent; second, the current density distribution is deduced from the cleaned magnetic field values.

7.4.1. From 'noisy' raw magnetic field values to 'cleaned' magnetic field values. This phase, sometimes called preprocessing, is devoted to the extraction of the magnetic field of the source under study from the whole population of magnetic sources, including also instrument noise sources. It should be remarked that the source under study is not a single source, such as a current dipole, but may be as well the current distribution over the whole brain. Generally speaking, any 'unwanted' magnetic fields, i.e. magnetic fields not generated by the source under study, are called 'noise', whereas the magnetic field generated by the source under study is called the 'signal'.

The first step is aimed at improving signal-to-noise ratio by excluding portions of highly noisy data. Two tasks are to be completed during this step, and since these tasks are not related to the particular source under study, they may just as well be accomplished by the DSPs before writing the data to the disk: (i) magnetic field values are examined in order to exclude that portion of the data corrupted by ADC overflows, noise or possible instrument failures; (ii) data contaminated by subject head movements or eye movements (if channels near the eyes are considered) are removed from the data set.

The next step is expected to maximize the signal-to-noise ratio by trying to separate, as much as possible, the signal from the noise using information on the specific source under study. MEG data cannot simply result from uncoordinated firing of single neurons. Indeed, we expect that neurons must partially synchronize their firing patterns to produce a meaningful and detectable magnetic field. A possible way to reveal synchronized neuron firing is bandpass filtering. Normal brain activity shows the existence of several rhythms: the alpha rhythm is comprised of components between 8 and 12 Hz; beta activity has a higher frequency, around 20 Hz. By proper bandpass filtering it is possible to discriminate the magnetic field generated by these natural rhythms from other magnetic fields due to other sources, either biological or not. An overview of the different approaches to neuromagnetic data handling, with special emphasis on the rhythmic activity of the human brain, may be found in the work of Elbert (1998).

In some cases it is possible to observe neural activity synchronization by supplying to the subject an external stimulus, or instructing the subject to perform a specific task, for example to move a finger. If this task is repeated many times, an average may be obtained over all the epochs. In this way only the magnetic field originated by a source correlated with the task is left unchanged, while all other signals are reduced by a factor $1/\sqrt{N}$, where N is the number of averages.

To clarify this procedure, let us describe a simple but typical session of evoked-field measurement. In this experiment the brain reaction to an external stimulus is measured. After data collection and removal of the components clearly not generated by the brain, the data are

averaged over all the stimuli presented to the subject. The averaging procedure cancels out all (noise) signals not phase locked to the stimulus, including the magnetic field still generated by intracerebral currents, but not related to the source activated by the stimulus. In this way the magnetic field values reflect only the source under study, i.e. that activated by the stimulus.

There are other cases when there is a need for specific data selection and extraction. For instance, when recording the magnetic field generated by spontaneous activity of an epileptic patient, the field values are sampled during a period of several minutes. Only during specific time windows is the pathological activity present, and these epochs must be identified correctly. Several tools are used in order to successfully reach this identification: correlation with a template, Fourier analysis, principal component analysis etc. Bandpass filtering also may be included in these tools as a procedure to separate noise from data.

7.4.2. From 'cleaned' magnetic field values to source characteristics. The final goal of the neuromagnetic technique, at least from the physicist's point of view, is often the determination of the current density distribution inside the brain. This task is not trivial since there is an infinite number of source configurations that can account for the same observed data. Several aspects related to the inverse-problem solution have been discussed already in section 5.

The results of this step are the ECD parameters (if a current dipole source is postulated), or current distribution inside the brain. It is worthwhile to remember that this current distribution is directly related to the underlined neuronal pools: therefore, locating an ECD inside the brain during a span of time means identifying a cluster of neurons and studying their activity during a specific mental task.

8. Applications of magnetoencephalography in basic research

In this and the following section we shall describe the most important achievements of MEG in basic neurophysiological studies, and in clinical studies.

8.1. Spontaneous brain activity

The cerebral activity of an animal at rest is characterized by an oscillatory activity, which has been observed at the whole-brain level, by means of EEG and MEG, as well as at the single-neural-cell level, by intracellular recordings. Neurophysiological techniques provide direct information on neuronal pool currents with sufficiently high temporal resolution to provide a deeper understanding of these oscillatory phenomena (Lopes da Silva 1987, 1991, Llinas 1988, Bullock 1993, Basar 1998).

8.1.1. Brain activity at rest. Cerebral activity at rest is characterized by oscillatory phenomena involving large synchronized neuronal pools, generated by intrinsic neural cell properties as well as by reverberant neural circuitry effects. Intrinsic oscillations are exhibited by the cerebral cortex and the thalamic nuclei mainly in the alpha range (Steriade and Llinas 1988, Hari and Salmelin 1997) and by the hippocampus with major activity in the theta range. Studies devoted to understanding the functional role of rhythmical spontaneous activity have so far revealed high specificity in different frequency ranges in relation to specific sensory–motor areas, in particular indicating oscillatory beta-range activity in the motor regions.

8.1.2. Functional synchronization/desynchronization of specific areas; cortico-cortical coherence. Resting rhythmic cerebral activity in different cortical areas is modified as a

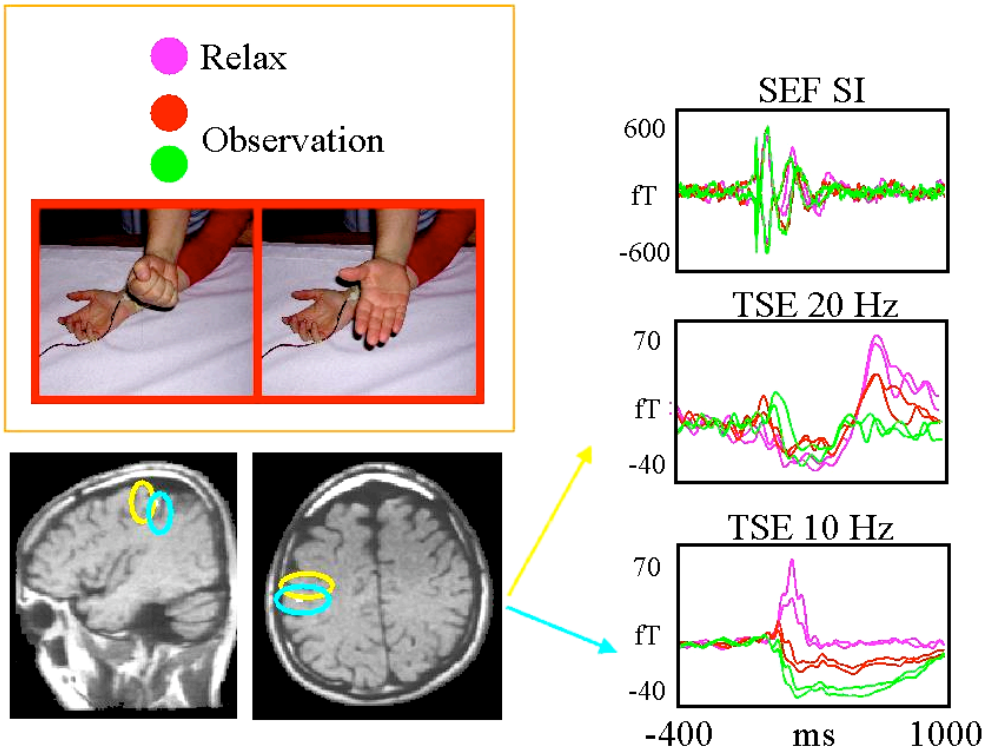

Figure 12. Cerebral activity during observation of simple movements performed by another person (experimental set in top left). Right, from the top: the somatosensory evoked fields (SEFs) recorded in the left primary sensorimotor area, and the evolution of the spontaneous activity (temporal spectrum evolution = TSE) at ≈20 Hz and at ≈10 Hz (same timescale). It is known that the oscillating activity around 20 Hz is generated mainly in the motor region (bottom left, yellow) and the 10 Hz characterizes the sensory areas (light blue). Note both ≈20 and ≈10 Hz activity reduction during observation, indicating the involvement of the primary somatosensory area in the observation condition.

consequence of specific sensory stimulation or motor action (Pfurtscheller and Lopes da Silva 1999). The term *desynchronization* refers to the cortical reactivity characterized by a power decrease within a specific frequency range when the cerebral region is stimulated by a sensory input or motor act. If the subject is lying relaxed with closed eyes and his cerebral activity is recorded, the described phenomenon is observed in occipital regions when the eyes are opened, in the temporal region when a sound is presented, as well as in parietal regions when a body district is moved or somatosensorially stimulated. Sensitivity of our sensory systems to stimulation at a particular frequency could indicate important features of brain responsiveness. The understanding of these mechanisms is of major importance *per se*, while desynchronization may also be used to characterize the partial involvement of specific areas during a cerebral process. In particular it has been demonstrated with this method that the motor system, including primary motor areas, is activated while we are observing an action performed by another person (figure 12).

Not only is the spontaneous activity modulated by incoming stimuli and cerebral processes, but the connectivity between cortical areas could functionally be correlated with time behaviour. A measurable parameter for describing functional coupling between different cerebral regions

is considered to be the coherence between signals recorded by MEG sensors covering different scalp areas (Gross *et al* 2001). In particular, merging of separate features into a single percept ('binding') has been observed to be associated with coherent gamma band activity across the involved cortical areas.

8.1.3. Corticomuscular coherence. Corticomuscular coherence between cerebral cortical rhythms and the surface electromyography (EMG) has been observed by means of electrocorticography, EEG and MEG (Salenius *et al* 1997). Corticomuscular coherence is a tool for the identification and characterization of cortical districts controlling a particular body district, based on amplitude and frequency selection. Temporal information about conduction times of rhythmic drive from motor cortex to motoneuronal pool based on phase difference dynamics could be obtained. This recently developed method could add deep insight to the cortical mechanisms and could help in discriminating the cortical from the spinal origin of motor control.

8.2. Evoked activity

MEG allows the three-dimensional localization of the cerebral sources activated by different kinds of stimulus in primary and secondary areas. Many characteristics of the sensory and motor functional connectivity could be investigated. Moreover, the direction of the cortical generator could be calculated and adjunctive neurophysiological information deduced about the involvement of specific areas (Pizzella *et al* 1999). As a third characteristic, the strength of the activated neuronal pool could be estimated, which represents an evaluation of the indicative number of neurons synchronously activated. In the following we describe the most important physiological functions investigated by means of MEG.

8.2.1. Somatosensory, auditory and visual evoked fields (SEFs–AEFs–VEFs).

(i) *SEFs.* Neuromagnetic responses to somatosensory stimulation have been among the more deeply investigated: the somatic–sensory pathway is characterized by the simplest peripheral-to-cortical projection among the various sensorial modalities, and for this reason it is the best 'first step' into the understanding of the processing ability of our brain. Since the hand is the most sensitive and the most precisely controlled district of our body, the central sensory and motor representations of the hand are very large. Thus, the very precise MEG description of the sensory representations of the different body parts is particularly detailed in the case of the hand district. The hand cortical representation is studied by mixed nerve or pure sensory electrical (Tecchio *et al* 1997, figure 13) and vibrational stimulation. The functional relationship between primary and nonprimary areas has also been addressed. The contribution of cerebral oscillations to evoked activity is again a physiological issue of great importance (Basar 1998, Curio 1999).

(ii) *AEFs.* With respect to tactile sensations, sound characteristics are elaborated more intensely both peripherally and centrally, before reaching our primary auditory cortex. Not only, in fact, is our ear able to perform a frequency analysis before the sound vibrations are transduced by the ciliate cells into electrical signals to be sent to the central system, but the neural pathway includes many synapsing relays before reaching the primary auditory cortex. To evaluate the integrity and characteristics of the subcortical tract, electrical recording methods have been suitably developed. MEG has been used largely to investigate the response of the auditory cortical regions to tone bursts or to temporally modulated stimulation. In particular, the tonotopical organization within the auditory cortex has

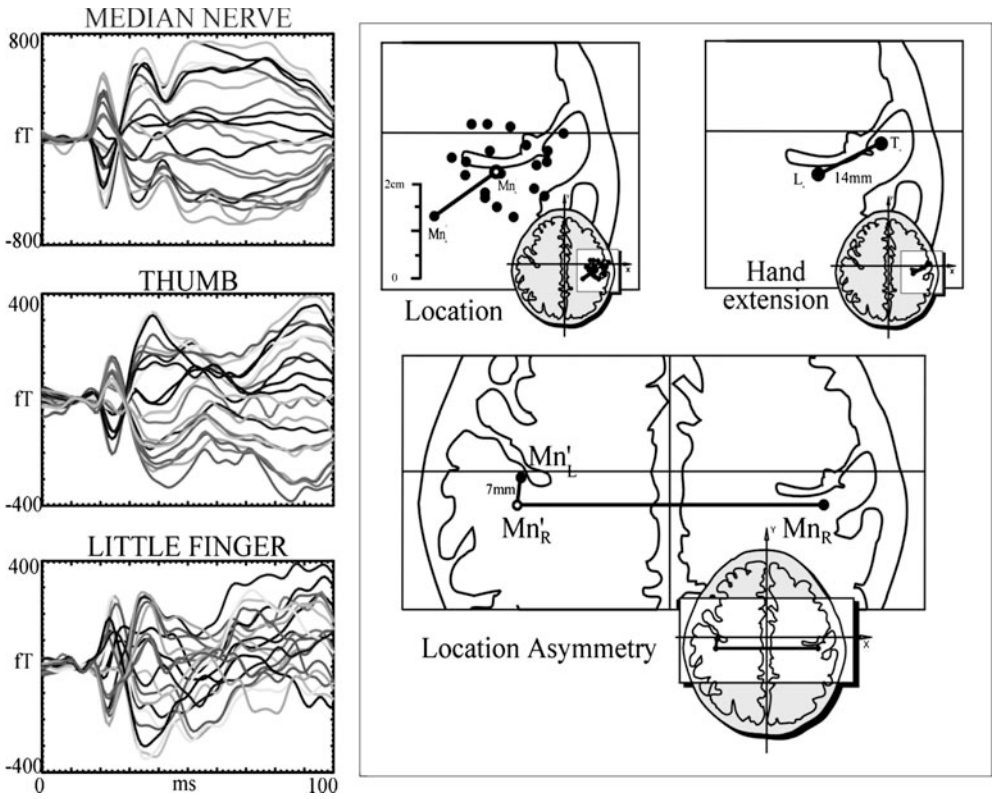

Figure 13. Left: superimposition of the signals from all sensors, in the 100 ms time interval starting with the electrical stimulation. SEF following separate stimulation of the median nerve, thumb and little finger. Right: illustrative drawing of an axial brain slice cutting the central sulcus, explaining three parameters describing the organization of the cortical hand representation: *location* represents the region where the cortical source related to each district is expected to fall in; *location asymmetry* defines the region where one district representation is expected to fall, once the location of the homologous district in the opposite hemisphere is known; *hand extension* evaluates the dimension of the cortical region devoted to the representation of the contralateral hand (Euclidean distance among thumb and little-finger representations).

been demonstrated (Romani *et al* 1982), and related to anatomical structures through the integration with MRI. Relationships between the auditory system and the human temporal perceptivity has been demonstrated with regard to persistence of memory trace and by focusing on frequency-dependent responses.

(iii) *VEFs.* The visual system, even more than the auditory system, performs a very sophisticated analysis of the spatial/intensity characteristics of light signals impinging onto the retina before transmitting them to the primary visual cortex. MEG has shown the retinotopic organization of the occipital primary visual cortex. Variations of the retinotopy in nonprimary visual cortex has also been shown. Once again the temporal characteristics of the cortical activation are mandatory in understanding the perception of both simple visual pattern stimuli and motion.

8.2.2. Motor evoked fields (MEFs). Despite the importance of motor control in human life, MEG has placed only a minor focus on this function as compared with the sensory elaboration

(nine versus 69 publications in the last two years). This is mainly related to the technical requirements in order to extract the cerebral activity controlling movements, i.e. the need to perform many very precise motor acts. This not only represents an experimental limitation for untrained subjects, but renders the method completely inapplicable to patients with any minor deficiency in motor performance. Moreover, in the 1980s, a new cortical stimulation method, namely transcranial magnetic stimulation (TMS), was introduced, making the investigation of primary motor cortical excitability more direct. Recently, new methods for the analysis of MEG signals characterizing motor control have been developed, which could open new applications of MEG, and a deeper understanding of cortical motor control. Moreover, these methods add new abilities for the study of sensory–motor integration. Nevertheless, many aspects of motor functions have so far been investigated, showing both cerebral activity characteristics during movement preparation and performance (Babiloni *et al* 1999), and motor-evoked sensory feedback. Cerebral motor system asymmetries related to cerebral dominance have been described. Cerebral oscillations, as one of the main mechanisms subtending sensorimotor integration, are under investigation.

8.2.3. Pain. Pain perception interacts deeply with the human motivational system, both exciting reaction movements and inhibiting acts, as well as modulating sensorial perceptivity. Human life can be completely modified and well-being destroyed by chronic pain. For these reasons nociceptive pathways have been investigated more and more. Pain has been observed, with MEG, to modify somatosensory processing and to be modified by attentive distracters.

8.2.4. Sensory–motor integration. Accumulated experience about separated sensory and motor functions has naturally driven the interest in sensory–motor integration. These two functions are so deeply related that our comprehension of observed situations, which we therefore perceive through our visual system, could be 'decoded' only via our motor system. It has been demonstrated in particular that when we observe another person performing a certain movement, the complex cerebral activity induced by this observation includes activation of part of the same cortical area as activated by our own motor act (Salenius 1999). Of primary importance is the coupling between the visual and sensorimotor systems: in fact visual feedback is the basis of precise motor act control. Interaction between sensory system excitability and motor performance has also been observed, demonstrating that auditory cortex is inhibited not only while the subject is speaking, but also during simple movement performance. Not only is sensory system activity modified by motor acts, but motor system excitability is altered by unexpected sensory stimuli.

8.2.5. Responses from subcortical structures and the cerebellum. Although MEG is less sensitive to deep sources than to cortical ones, a specific data analysis method (signal space projection—SSP), that postulates activity in a specific deep brain region, permits one to extract temporal waveforms and oscillation power from thalamic, hippocampal and cerebellar activities (Tesche and Karhu 2000).

8.3. Cognitive functions

8.3.1. Attention, perceptive and discriminative functions. Investigation of human sensorial systems has indicated their ability not only to transduce physical signals (light, sounds, pressure and temperature variations, chemical substances) into electrochemical signals to our central elaborating regions, but also that the sensory systems themselves perform high-level processing

with discriminative abilities (Sams *et al* 1991), which could be modulated significantly by attention. Moreover a large body of evidence indicates auditory system ability in temporal discrimination. Conscious perception has been demonstrated to take place at higher levels with respect to the systemic cortices (one example for the auditory system is given in the work of Tecchio *et al* (2000a)), although a relationship between primary cortical activity and perceptual systemic abilities has been found (Tononi *et al* 1998).

8.3.2. Memory. Although memory is probably the most basic function of our minds, in the sense that every functional process is due to memory abilities in establishing neural network structures during development and in the continuous process of relevant/non relevant stimuli discrimination, its study is not so simple at the whole-brain level as it is at single-cell level. As more powerful means of signal analysis have increased our ability to extract information about functional properties from our cerebral signals, interest has focused on memory functions (Glantz 1998, Okada and Salenius 1998). Mnemonic functions have been suggested to be supported by the hippocampal theta rhythm (Tesche and Karhu 2000).

8.3.3. Mental imagery. Investigation of sensorial and motor systems and their interaction mechanisms have provided the necessary basis for understanding more complex cerebral functions. It is thought that investigation of our brain's processes during imagery of simple tasks or objects may help in understanding more complex and 'human elective' deductive abilities. These processes, that could hardly be separated into different steps, are an elective application for integrative studies with multimodal functional imaging techniques.

8.3.4. Language function. As with memory and mental imagery, language function is obviously of major importance for human life. Its understanding is mandatory both at the level of explaining how our mind works and for making it possible to develop both suitable teaching methods for students and rehabilitation procedures in pathological situations. In this respect, MEG has been of primary importance and the great quantity of published works in the last years testifies that MEG researchers have focused on this topic (30 papers in the last two years, around 16% of all the physiological studies, and half of all the studies on sensorimotor-evoked activities). Investigation of cerebral regions involved in language encoding and comprehension has shown hemispheric laterality. Different steps of language processing were focused on preattentive processing, discrimination between perception and recognition of word, between word or context comprehension (Helenius *et al* 1998), and comprehension of the whole sentence. Visually presented language has also been investigated, as has processing during language production in parallel to processing during verbal presentation. The particular structure of Japanese language has required many specific studies. Cerebral characterization related to altered production of speech has been demonstrated (Salmelin *et al* 1998).

8.3.5. Emotion. The experience of emotion represents the base of the whole human system for learning and motivation, by modulating both sensory and pain perception as well as motor control through the reticular system and defining neurotransmitter release and effectiveness. The modern theories about human well-being have pointed out the necessity of the integrity between emotional requirements and personal choice about everyday life organization. Cerebral correlations with such a wide experience is of great interest. Once again, when the process is very complex, involving deep sources and modulating the whole brain activity, it is very difficult to separate different aspects. Comparison between recognition of unemotional complex objects and emotional faces has been investigated. Within emotional experience,

comparison between positive and negative emotion has been performed by integrating MEG and fMRI.

8.3.6. Consciousness. MEG researchers recently started investigating cerebral regions or properties related to conscious perception: it has been shown that the sensory cortex may receive the information needed to discriminate different stimuli, but the corresponding higher-level elaborating areas are not 'trained' to consciously perceive these stimuli as different (Tecchio *et al* 2000a). Although the systemic cortex may have a higher sensitivity than our consciousness system, the conscious perception of a sensorial stimulus produces an increased synchronization in the whole cortex, in specific frequency ranges, compared with the unconscious perception of an identical stimulus (Tononi *et al* 1998).

8.4. Physiological plasticity

Recent studies at cellular and systemic levels have shown human adult brain ability in modifying its functional activation properties in relation to modifications of peripheral or central homeostasis. In the short-term timescale (i.e. minutes–a few hours) it has been demonstrated that the cortical representation of one body district could invade the neighbouring ones if the latter are deprived of their physiological sensorial input (Rossini *et al* 1994, figure 14). On longer timescales, central cortical representation changes have been observed in physiological conditions, as an effect of skillful movement learning: for example, simple sounds in the auditory cortical regions are more represented in musicians (Pantev *et al* 1998).

9. Clinical applications of magnetoencephalography

9.1. Pre-surgical mapping: visual, auditory, somatosensory and motor cortex characterization

MEG's ability to spatially identify functionally relevant neuronal areas has its primary application to pre-operative analysis, in order to minimize surgical effects on sensorimotor functionality. It is possible to indicate with high resolution via MRI anatomical images the location of the functionally activated area in the individual stereotactic coordinate system. It has been also used to define a functional risk profile in the selection for surgery of a patient with brain lesions (tumours or arteriovenous malformations): the benefits/risk ratio evaluation has been successfully applied (Hund *et al* 1997).

9.2. Identification of epileptogenic areas: single interictal spikes and seizure generator identification

Spatial identification of epileptogenic foci is one main opportunity for MEG, due to the direct measurement of the effect of the paroxystic electrical neuronal activity. Single interictal spike generators have been identified spatially, also in relation to electrocorticogram recordings. This could help in discriminating situations with different neuroradiological and clinical evaluations. Extremely relevant to presurgical evaluation and for the comparison with intracerebral presurgical recordings is the ability to localize the seizure generator: this could be obtained during subclinical ictal activity or in those situations where the critical event does not involve a motor discharge.

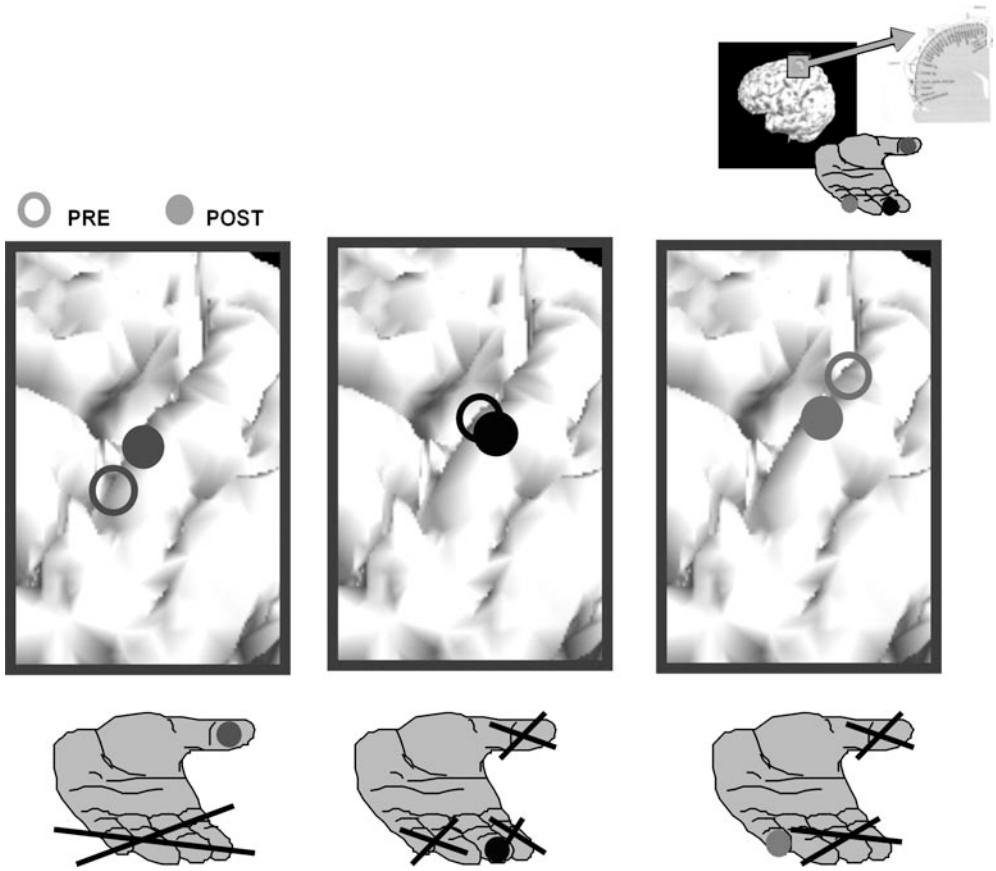

Figure 14. The cortical representation of one digit 'invades' the region devoted to the others, if sensory inflow form the latter is reduced by anaesthetic block. In the top right inset, 'homuncular' distribution of the cortical representation of the hand is discriminated by the MEG method.

9.3. Plasticity following central and peripheral lesions

We mentioned in section 8.4 that the human adult brain maintains the ability to change the functional organization of neuronal pools following training periods or alteration of the sensory input. In particular reorganizations have been observed following partial deprivation of the sensorial inflow to the auditory system (Tecchio *et al* 2000b, figure 15). In the somatosensory cortical representation, distinct somatotopical representations appeared following surgical separation of webbed fingers (syndactyly) compared with before surgery, when the two fingers had shrunken representations. These abilities are of great importance in the reaction to peripheral or cerebral lesions. In fact they subtend partially to the ability to recover after injury. In stroke patients, cerebral involvement of areas outside the region reached by dense projections from the hand have been characterized in patients showing partial sensorimotor recovery. The re-established functional setting does not allow functionality as before the ischaemic event (Rossini *et al* 1998a, 2001, figure 16). Cortical reorganizations may also be disadaptive: it has been hypothesized that they contribute to pain symptoms, for example in phantom pain (Flor *et al* 1995).

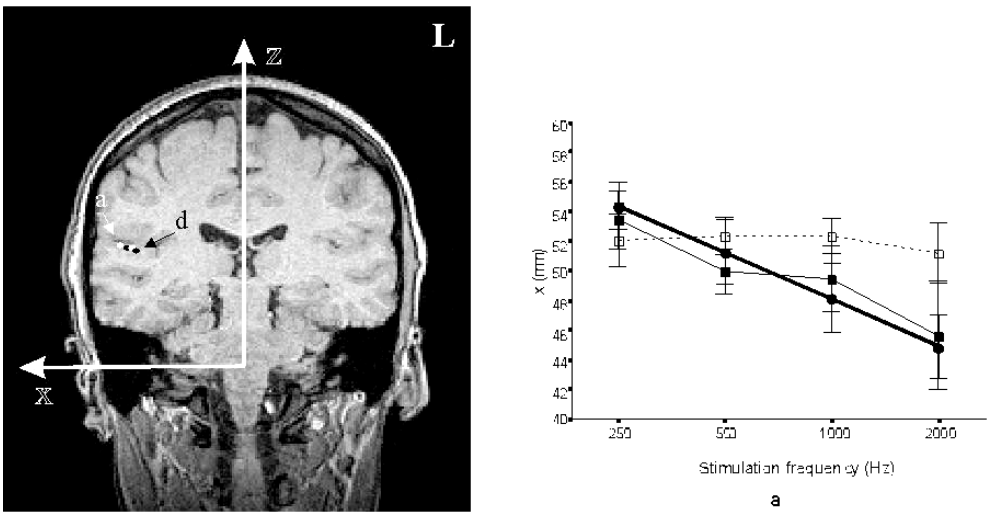

Figure 15. Left: main auditory cortical source positions in one control subject, in response to 250 (a), 500, 1000, 2000 (d) Hz tone bursts, showing the relation between ECD depth and the x-coordinate. Superposition with MRI confirms dipole positioning within the depth of the supratemporal Silvian fissure, with high-frequency tones representing deeper (tonotopic distribution). Right: tonotopic extension in normal-hearing subjects (closed circle) and patients before (open square) and after surgery (closed square).

9.4. Psychiatric studies

Many indications about our mind's functional capabilities arise from its dysfunction. For this reason, and to search for therapeutic treatments of psychiatric diseases, many studies are devoted to these pathologies. In the first direction, many papers focus on language disorders: dyslexia (Helenius *et al* 1999) or reading difficulties. In schizophreniform disorders anomalous cerebral asymmetry has been described, and the first reports on pharmacological effects have appeared. Developmental disorders have been investigated in particular in autistic subjects. Cerebral characterization during sensorial hallucinations has shown right auditory cortex dysfunction during musical hallucinations in an old woman who was otherwise cognitively intact. Anomalous brain asymmetry has been observed in subjects suffering bipolar depression.

9.5. Neurological dysfunction studies

Cerebral activity is altered in patients affected by neurological diseases with different etiologies, and some new insight could clarify subtending mechanisms. Alzheimer's disease is a pathology with growing social and economic impact, espescially with the aging of the population. This disease has been studied by means of MEG to relate metabolic, anatomical and neurophysiological alterations.

In stroke patients, not only plastic effects, see section 9.3, but also significant excitability alterations have been observed in both the affected and unaffected hemispheres (Rossini *et al* 1998a, figure 16; 1998b).

Thalamic functions have been more deeply characterized by studying patients with thalamic infarctions. Thalamocortical projections contribution with modulation in frequency activity has been characterized in parkinsonian patients (Volkmann *et al* 1996) as have alterations in frequency responsiveness observed in other cerebral lesions.

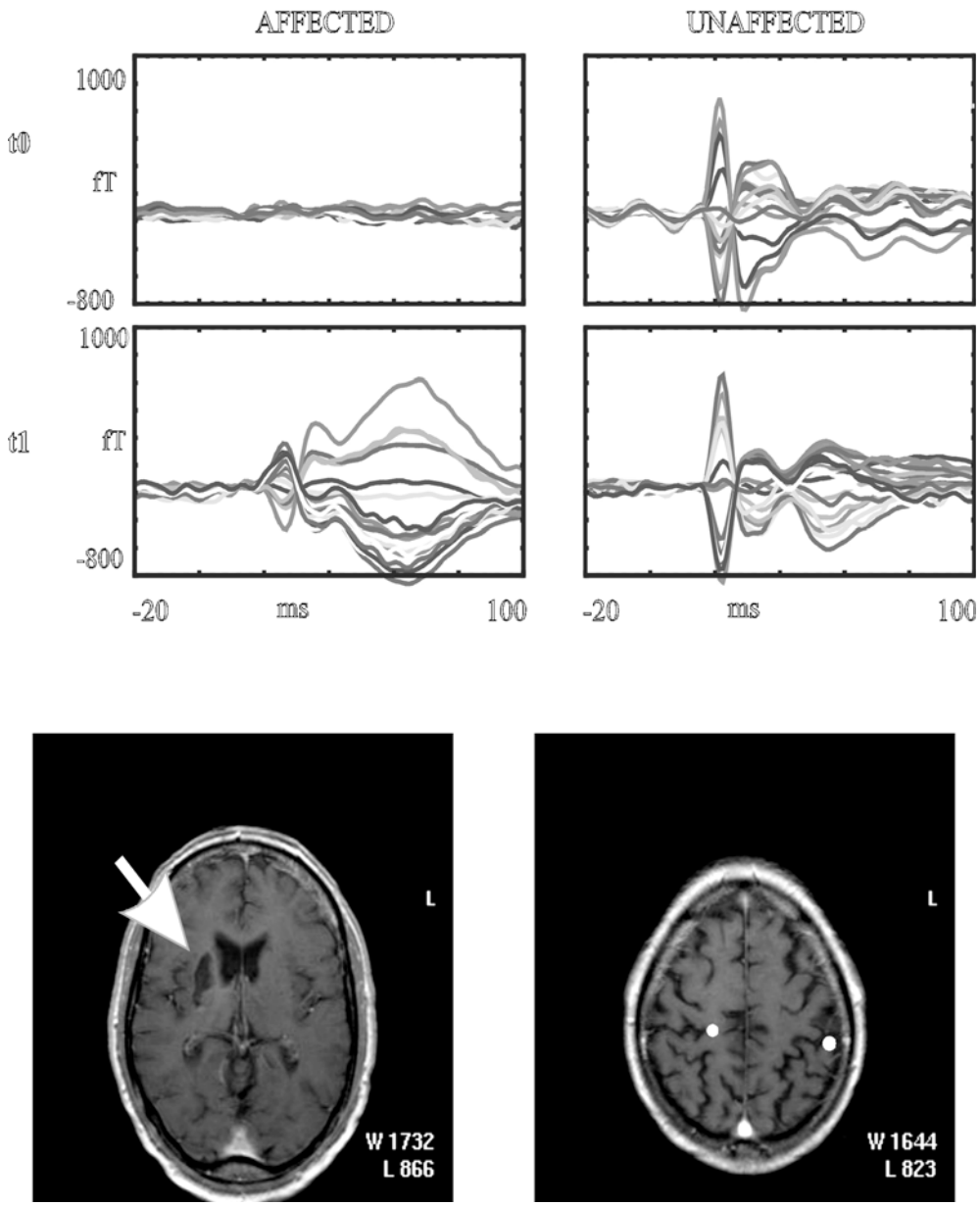

Figure 16. Top: superimposition of the 25 recording channels in the [−20, 100] ms time interval, showing SEF abnormalities in one patient affected by a large lesion involving the globus pallidus, putamen and internal capsule of the right hemisphere. SEFs are strongly depressed from the lesioned hemisphere and enhanced from the unaffected hemisphere at time of the ischaemic event (t_0). Recovery at 6 months (t_1) later shows SEF recovery with an asymmetry of the responding cortical region. Bottom: MRI image showing the lesion site and MRI/MEG integration for the anatomical identification of the functionally activated neuronal pools.

10. Conclusion

In this review we have tried to inform the reader of the basic principles, the methods, and the applications of MEG. We by no means claim to have been exhaustive, in the sense of having

Table 1. MEG main findings in basic research and clinical applications.

General topic	Specific topic	Method of analysis	Main results
Spontaneous brain activity	Brain activity at rest	Frequency spectra. Cerebral topography in different bands.	Characterization of different areas through their spontaneous activity (Hari and Salmelin 1997, Tesche and Karhu 2000). Spectral and topographical alterations in neurological pathologies (Volkmann *et al* 1996).
	Synchronization/ desynchronization	Time course of rhythmic activity modulation in relation to specific cerebral processes.	Involvement of different areas during specific cerebral tasks (Salenius 1999).
	Cortico-cortical coherence	Frequency specificity. Coherence topography.	Behaviour emerges also through variation of connectivity between Cortical areas (Gross *et al* 2001). Consciousness relates to coherence pattern through the whole head (Tononi *et al* 1998).
	Cortico-muscular coherence	Frequency specificity. Coherence topography. Phase shift.	Discrimination of cortical contribution to motor control (Salenius *et al* 1997). Characterization of cortical involvement in myclonus and Parkinson diseases (Brown *et al* 1999, Volkmann *et al* 1996).
	Epileptic activity	Frequency content. Localization.	Identification of epileptogenic areas (Nishitani *et al* 1999).
Evoked activity	SEF–AEF–VEF MEF	Morphological characteristics of the evoked responses and readiness activity Identification of position, strength and direction of the cortical activated sources.	Characterization of cerebral areas in relation to their functional role (Hari *et al* 1980, Tecchio *et al* 1997). Presurgical mapping in patient undergoing neurosurgical treatment (Hund *et al* 1997). Characterization of cortical reorganization in consequence of central or peripheral lesions (Flor *et al* 1995, Rossini *et al* 2001, Tecchio *et al* 2000b).
Cognitive functions	Discrimination and attention		Characterization of involvement of different levels of sensory systems during discrimination tasks (Sams *et al* 1991).
	Memory		Identification of different structures involved in memory processes (Okada and Salenius 1998. Tesche and Karhu 2000). Alteration in working- and long-term-memory functions in neurological and psychiatric diseases (Kissler *et al* 2000).
	Language function		Cerebral regions involved in language encoding and comprehension (Helenius *et al* 1998, Salmelin *et al* 1998) Investigation of reading difficulties or dyslexia (Helenius *et al* 1999).
	Consciousness		Characterization of cerebral activity subtending conscious perception (Tononi *et al* 1998, Tecchio *et al* 2000a).

cited all the original work in each topic. This would have taken too long to do, and, in our opinion, would have been outside the scope of this review. There are, at the present time, many groups working in MEG, and many different solutions to the theoretical and practical problems of this technique have been implemented. We apologize if the work of some people has been omitted. We hope, however, to have pointed out the main issues that have been addressed, and the common solutions that have been adopted. Concerning the applications of this technique, there are now many published works, of which we have cited only a few. This is a clear indication of the acceptance gained by MEG, at least in research centres. Clinical applications are now increasing, and quite a few centres have now adopted MEG as a standard tool for preoperative noninvasive investigation.

In the recent past, MEG has benefited from MRI for the construction of numerical models of the head for data analysis, as well as a means for the visualization of the estimated neural currents in combination with the subject's cerebral anatomy. The increasingly wide spreading of MRI makes this combination possible, and the nonavailability of an MRI scanner is no longer a problem for researchers working in MEG.

Although new techniques for brain imaging have emerged—such as functional MRI (fMRI) or positron emission tomography (PET)—MEG remains the only approach with a very high time resolution, limited in practice only by the data acquisition system. This feature indicates that for the near future an avenue for the development of MEG will be its combination with the above-mentioned techniques, in particular fMRI, that is now easily performed on conventional scanners and entails a relatively comfortable examination procedure for subjects as well as for patients. fMRI has a relatively high spatial resolution, of the order of one millimetre (although electric activity is not observed directly), but a poor temporal resolution, limited by haemodynamics. Indeed, it will be possible to improve MEG inverse solutions by using fMRI-derived information to constrain the former. On the other hand, the MEG time course will make it possible to perform dynamic studies with fMRI with a time resolution on the same scale as neurophysiological events. The combination of the two techniques poses a number of problems that are practical and technical, as well as theoretical, for the correct merging of these two types of datum. Many research centres around the world are engaging in this work, the idea of which is to take advantage of many available neuroimaging techniques to extract from their combination the information that each alone cannot provide. Although this field is in its infancy, there is much excitement and activity, and a detailed account could well be the topic of another review article.

References

Babiloni C, Carducci F, Pizzella V, Indovina I, Romani G L, Rossini P M and Babiloni F 1999 Bilateral neuromagnetic activation of human primary sensorimotor cortex in preparation and execution of unilateral voluntary finger movements *Brain Res.* **827** 234–6

Babiloni F, Carducci F, Cincotti F, Del Gratta C, Pizzella V, Romani G L, Rossini P M, Tecchio F and Babiloni C 2001 Linear inverse source estimate of combined EEG and MEG data related to voluntary movements *Hum. Brain Mapping* **14** 197–209

Barnard A C L, Duck I M, Lynn M S and Timlake W P 1967 The application of electromagnetic theory to electrocardiology II *Biophys. J.* **7** 463–91

Barth D S, Sutherling W, Engel J Jr and Beatty J 1982 Neuromagnetic localization of epileptiform spike activity in the human brain *Science* **218** 891–4

——1984 Neuromagnetic evidence of spatially distributed sources underlying epileptiform spikes in the human brain *Science* **223** 293–6

Basar E 1998 *Brain Function and Oscillations* ed H Haken (Berlin: Springer)

Bork J, Hahlbohm H-D, Klein R and Schnabel A 2001 *Proc. 12th Int. Conf. on Biomagnetism (Helsinki, 2000)* ed J Nenonen, R J Ilmoniemi and T Katila at press

Brenner D, Williamson S J and Kaufman L 1975 Visually evoked magnetic fields of the human brain *Science* **190** 480–2

Brown P, Farmer S F, Halliday D M, Marsden J and Rosenberg J R 1999 Coherent cortical and muscle discharge in cortical myoclonus *Brain* **122** 461–72

Bullock T H 1993 *How do Brains Work?* (Basle: Birkhauser)

Carelli P, Castellano M G, Torrioli G and Leoni R 1998 Low noise multiwasher superconducting interferometer *Appl. Phys. Lett.* **72** 115–17

Carelli P and Pizzella V 1992 Biomagnetism: an application of superconductivity *Supercond. Sci. Technol.* **5** 407–20

Chapman R M, Romani G L, Barbanera S, Leoni R, Modena I, Ricci G B and Campitelli F 1983 SQUID instrumentation and the relative covariance method for magnetic 3-D localization of pathological cerebral sources *Lett. Nuovo Cimento* **38** 549

Cincotti F, Babiloni C, Carducci F, Del Gratta C, Romani G L, Rossini P M and Babiloni F 2001 The use of fMRI priors for the estimation of cortical activity with high resolution EEG *Electromagnetics* **21** 579–92

Clarke J 1996 SQUID fundamentals *SQUID Sensors: Fundamentals, Fabrication and Applications* ed H Weinstock (Dordrecht: Kluwer) pp 1–62

Cohen D 1968 Magnetoencephalography: evidence of magnetic fields produced by alpha-rhythm currents *Science* **161** 784–6

——1972 Magnetoencephalography: detection of the brain's electrical activity with a superconducting magnetometer *Science* **175** 664–6

Cohen D, Edelsack E A and Zimmerman J E 1970 Magnetocardiograms taken inside a shielded room with a superconducting point contact magnetometer *Appl. Phys. Lett.* **16** 278–80

Curio G 1999 High frequency (600 Hz) bursts of spike-like activities generated in the human cerebral somatosensory system *Electroencephalogr. Clin. Neurophysiol. Suppl.* **49** 56–61

Della Penna S, Del Gratta C, Granata C, Pasquarelli A, Pizzella V, Rossi R, Russo M, Torquati K and Ernè S N 2000 Biomagnetic systems for clinical use *Phil. Mag.* B **80** 937–48

Drung D 1996 Advanced SQUID read-out electronics *SQUID Sensors: Fundamentals, Fabrication and Applications* ed H Weinstock (Dordrecht: Kluwer) pp 63–116

Elbert T 1998 Neuromagnetism *Magnetism in Medicine* ed W Andrä and H Nowak (Berlin: Wiley) pp 190–261

Ferguson A S, Zhang X and Stroink G 1994 A complete linear discretisation for calculating the magnetic field using the boundary element method *IEEE Trans. Biomed. Eng.* **41** 455–60

Flor H, Elbert T, Knecht S, Wienbruch C, Pantev C, Birbaumer N, Larbig W and Taub E 1995 Phantom-limb pain as a perceptual correlate of cortical reorganization following arm amputation *Nature* **375** 482–4

Geselowitz D B 1967 On bioelectric potentials in an inhomogeneous volume conductor *Biophys. J.* **7** 1–11

——1970 On the magnetic field generated outside an inhomogeneous volume conductor by internal current sources *IEEE Trans. Magn.* **6** 346–7

Glantz J 1998 Magnetic brain imaging traces a stairway to memory *Science* **280** 37

Gross J, Kujala J, Hamalainen M, Timmermann L, Schnitzler A and Salmelin R 2001 Dynamic imaging of coherent sources: studying neural interactions in the human brain *Proc. Natl Acad. Sci. USA* **98** 694–9

Gulrajani R M 1998 *Bioelectricity and Biomagnetism* (New York: Wiley)

Hämäläinen M, Hari R, Ilmoniemi R, Knuutila J and Lounasmaa O 1993 Magnetoencephalography—theory, instrumentation, and applications to noninvasive studies of the working human brain *Rev. Mod. Phys.* **65** 413–97

Hämäläinen M and Ilmoniemi R 1984 Interpreting the magnetic field of the brain: estimates of current distributions *Report* TKK-F-A559 Helsinki University of Technology

——1994 Interpreting magnetic fields of the brain: estimates of current distributions *Med. Biol. Eng. Comput.* **32** 35–42

Hämäläinen M S and Sarvas J 1989 Realistic conductivity geometry model of the human head for interpretation of neuromagnetic data *IEEE Trans. Biomed. Eng.* **36** 165–71

Hansen P C 1992 Analysis of discrete ill-posed problems by means of the L-curve *SIAM Rev.* **34** 561–80

Hari R, Aittoniemi K, Jarvinen M-L, Katila T and Varpula T 1980 Auditory evoked transient and sustained magnetic fields of the human brain: localization of neural generators *Exp. Brain Res.* **40** 237–40

Hari R and Salmelin R 1997 Human cortical oscillations: a neuromagnetic view from the skull *Trends Neurosci.* **20** 44–9

Helenius P, Salmelin R, Service E and Connolly J F 1998 Distinct time courses of word and context comprehension in the left temporal cortex *Brain* **121** 1133–42

Helenius P, Tarkiainen A, Cornelissen P, Hansen P C and Salmelin R 1999 Dissociation of normal feature analysis and deficient processing of letter-strings in dyslexic adults *Cereb. Cortex* **9** 476–83

Helmholtz H von 1853 Über einige Gesetze der Verteilung elektrischer Ströme in körperlichen Leitern, mit Anwendung auf die tierisch-elektrischen Versuche *Ann. Phys. Chem.* **89** 211–33

——1853 Über einige Gesetze der Verteilung elektrischer Ströme in körperlichen Leitern, mit Anwendung auf die tierisch-elektrischen Versuche *Ann. Phys. Chem.* **89** 353–77

Hund M, Rezai A R, Kronberg E, Cappell J, Zonenshayn M, Ribary U, Kelly P J and Llinas R 1997 Magnetoencephalographic mapping: basic of a new functional risk profile in the selection of patients with cortical brain lesions *Neurosurgery* **40** 936–43

Ilmoniemi R J, Hämäläinen M S and Knuutila J 1985 *Biomagnetism: Applications and Theory* ed H Weinberg, G Stroink and T Katila (Oxford: Pergamon) pp 278–82

Jackson J D 1975 *Classical Electrodynamics* 2nd edn (New York: Wiley)

Josephson B D 1962 Possible new effects in superconductive tunnelling *Phys. Lett.* **1** 251–3

Katila T and Karp P 1983 Magnetocardiography: morphology and multipole presentations *Biomagnetism: an Interdisciplinary Approach* ed S J Williamson, G L Romani, L Kaufman and I Modena (New York: Plenum) pp 237–63

Kissler J, Muller M M, Fehr T, Rockstroh B and Elbert T 2000 MEG gamma band activity in schizophrenia patients and healthy subjects in a mental arithmetic task and at rest *Clin. Neurophysiol.* **111** 2079–87

Koester J 1985 Resting membrane potential and action potential *Principles of Neural Science* 2nd edn, ed E R Kandel and H J Schwartz (Amsterdam: Elsevier) pp 49–57

Lawson C L and Hanson R J 1974 *Solving Least Squares Problems* (Englewood Cliffs, NJ: Prentice-Hall)

Llinas R 1988 The intrinsic electrophysiological properties of mammalian neurons: insight into nervous system function *Science* **242** 1654–64

Lopes da Silva F H 1987 Dynamics of EEGs as signals of neuronal populations: models and theoretical considerations *Electroencephalography: Basic Principles, Clinical Applications and Related Fields* ed E Niedermeyer and F H Lopes da Silva (Baltimore: Urban and Schwarzenberg) pp 15–28

Lopes da Silva F H 1991 *Electroencephalogr. Clin. Neurophysiol.* **79** 81–93

Lynn M S and Timlake W P 1968 The use of multiple deflations in the solution of singular systems of equations with application to potential theory *SIAM J. Numer. Anal.* **5** 303–22

Malmivuo J and Plonsey R 1995 *Bioelectromagnetism* (New York: Oxford University Press)

Marquardt D W 1963 An algorithm for least squares estimation of non linear parameters *J. Soc. Ind. Appl. Math.* **11** 431–41

McKay J, Vrba J, Betts K, Burbank M B, Lee S, Mori K, Nonis D, Spear P and Uriel Y 1993 *Proc. 1993 Can. Conf. on Electrical and Computer Engineering* vol 2 pp 1090–3

Miller K 1970 Least squares methods for ill-posed problems with a prescribed bound *SIAM J. Math. Anal.* **1** 52–74

Modena I, Ricci G B, Barbanera S, Leoni R, Romani G L and Carelli P 1982 Biomagnetic measurements of spontaneous brain activity in epileptic patients *Electroencephalogr. Clin. Neurophysiol.* **54** 622–8

Mosher J C, Lewis P S and Leahy R M 1992 Multiple dipole modeling and localization from spatio-temporal MEG data *IEEE Trans. Biomed. Eng.* **39** 541–57

Munck J C de 1990 The estimation of time varying dipoles on the basis of evoked potentials *Electroencephalogr. Clin. Neurophysiol.* **77** 156–60

——1992 A linear discretisation of the volume conductor boundary integral equation using analytically integrated elements *IEEE Trans. Biomed. Eng.* **39** 986–90

Nelder J A and Mead R 1965 A simplex method for function minimization *Comput. J.* **7** 308–13

Nenonen J, Ilmoniemi R J and Katila T (ed) 2000 *Proc. 12th Int. Conf. on Biomagnetism (Helsinki, 2000)* at press

Nishitani N, Ikeda A, Nagamine T, Honda M, Mikuni N, Taki W, Kimura J and Shibasaki H 1999 The role of the hippocampus in auditory processing studied by event-related electric potentials and magnetic fields in epilepsy patients before and after temporal lobectomy *Brain* **122** 687–70

Nolte G and Curio G 1997 On the calculation of magnetic fields based on multipole modeling of focal biological current sources *Biophys. J.* **73** 1253–62

Nowak H 2000 Data presented at BIOMAG 2000 Conference, Helsinki, 13–17 August

Okada Y C, Salenius S 1998 Roles of attention, memory, and motor preparation in modulating human brain activity in a spatial working memory task *Cereb. Cortex* **8** 80–96

Oostendorp T F and Oosterom A van 1989 Source parameter estimation in inhomogeneous volume conductors of arbitrary shape *IEEE Trans. Biomed. Eng.* **36** 382–91

Oosterom A van and Strackee J 1983 The solid angle of a plane triangle *IEEE Trans. Biomed. Eng.* **30** 125–6

Oppenheim A V and Schafer R W 1989 *Discrete-time Signal Processing* (Englewood Cliffs, NJ: Prentice-Hall)

Pantev C, Oostenveld R, Engelien A, Ross B, Roberts L E and Hoke M 1998 Increased auditory cortical representation in musicians *Nature* **392** 811–3

Pascual-Marqui R D, Michel C M and Lehman D 1995 Low resolution electromagnetic tomography: a new method for localising electrical activity in the brain *Int. J. Psychophysiol.* **18** 49–65

Pasquarelli A, Kammrath H, Tenner U and Erné S N 1999 *Recent Advances in Biomagnetism* ed T Yoshimoto *et al*

(Sendai: Tohoku University Press) pp 55–8
Pfurtscheller G and Lopes da Silva F H 1999 Event-related EEG/MEG synchronization and desynchronization: basic principles *Clin. Neurophysiol.* **110** 1842–57
Pizzella V, Tecchio F, Romani G-L and Rossini P M 1999 Functional localization of the sensory hand area with respect to the motor central gyrus knob *Neuroreport* **10** 1–6
Pizzella V, Della Penna S, Del Gratta C and Romani G L 2001 SQUID systems for biomagnetic imaging *Supercond. Sci. Technol.* **14** R79–114
Romani G L, Williamson S J and Kaufman L 1982 Tonotopic organization of the human auditory cortex *Science* **216** 1339–40
Rossini P M, Caltagirone C, Castriota-Scanderbeg A, Cicinelli P, Del Gratta C, Demartin M, Pizzella V, Traversa R and Romani G L 1998b Hand motor cortical area reorganization in stroke: a study with fMRI, MEG and TCS maps *Neuroreport* **9** 2141–6
Rossini P M, Martino G, Narici L, Pasquarelli A, Peresson M, Pizzella V, Tecchio F, Torrioli G and Romani G L 1994 Short-term brain 'plasticity' in humans: transient finger representation changes in sensory cortex somatotopy following ischemic anaesthesia *Brain Res.* **642** 169–77
Rossini P M, Tecchio F, Pizzella V, Lupoi D, Cassetta E and Paqualetti P 2001 Interhemispheric differences of sensory hand areas after monohemispheric stroke: MEG/MRI integrative study *Neuroimage* **14** 474–85
Rossini P M, Tecchio F, Pizzella V, Lupoi D, Cassetta E, Pasqualetti P, Romani G L and Orlacchio A 1998a On the reorganization of sensory hand areas after mono-hemispheric lesion: a functional (MEG)/anatomical (MRI) integrative study *Brain Res.* **782** 153–66
Salenius S 1999 'Human see, human do' cortex *Mol. Psychiatr.* **4** 307–9
Salenius S, Schnitzler A, Salmelin R, Jousmaki V and Hari R 1997 Modulation of human cortical rolandic rhythms during natural sensorimotor tasks *Neuroimage* **5** 221–8
Salmelin R, Schnitzler A, Schmitz F, Jancke L, Witte O W and Freund H J 1998 Functional organization of the auditory cortex is different in stutterers and fluent speakers *Neuroreport* **9** 2225–9
Sams M, Kaukoranta E, Hamalainen M and Naatanen R 1991 Cortical activity elicited by changes in auditory stimuli: different sources for the magnetic N100m and mismatch responses *Psychophysiology* **28** 21–8
Sarvas J 1987 Basic mathematical and electromagnetic concepts of the biomagnetic inverse problem *Phys. Med. Biol.* **32** 11–22
Scherg M 1991 Fundamentals of dipole source analysis *Auditory Evoked Magnetic Fields and Electric Potentials (Advances in Audiology Vol. 6)* ed F Grandori, M Hoke and G L Romani (Basel: Karger) pp 40–69
Steriade M and Llinas R R 1988 The functional states of the thalamus and the associated neuronal interplay *Physiol. Rev.* **68** 649–742
Tecchio F, Bicciolo G, De Campora E, Pasqualetti P, Pizzella V, Indovina I, Cassetta E, Romani G-L and Rossini P M 2000b Tonotopic cortical changes following stapes substitution in otosclerotic oatients: a magnetoencephalographic study *Hum. Brain Mapping* **10** 28–38
Tecchio F, Rossini P M, Pizzella V, Cassetta E and Romani G L 1997 Spatial properties and interhemispheric differences of the sensory hand cortical representation: a neuromagnetic study. *Brain Res.* **767** 100–8
Tecchio F, Salustri C, Thaut M H, Pasqualetti P and Rossini P M 2000a Conscious and preconscious adaptation to rhythmic auditory stimuli: a magnetoencephalographic study of human brain responses *Exp. Brain Res.* **135** 222–30
ter Brake H J M, Huonker R and Rogalla H 1993 New results in active noise compensation for magnetically shielded rooms *Meas. Sci. Technol.* **4** 1370–5
Tesche C D and Karhu J 2000 Theta oscillations index human hippocampal activation during a working memory task *Proc. Natl Acad. Sci. USA* **97** 919–24
Tikhonov A N and Arsenin V Y 1977 *Solution of Ill-Posed Problems* (Washington, DC: Winston)
Titomir L I and Kneppo P 1994 *Bioelectric and Biomagnetic Fields. Theory and Applications in Electrocardiology* (Boca Raton, FL: Chemical Rubber Company)
Tononi G, Srinivasan R, Russell D P and Edelman G M 1998 Investigating neural correlates of conscious perception by frequency-tagged neuromagnetic responses *Proc. Natl Acad. Sci. USA* **95** 3198–203
Tripp J H 1983 Physical concepts and mathematical models *Biomagnetism: an Interdisciplinary Approach* ed S J Williamson, G L Romani, L Kaufman and I Modena (New York: Plenum) pp 101–39
Volkmann J, Joliot M, Mogilner A, Ioannides A A, Lado F, Fazzini E, Ribary U and Llinas R 1996 Central motor loop oscillations in parkinsonian resting tremor revealed by magnetoencephalography *Neurology* **46** 1359–70
Vrba J 1996 *SQUID Sensors: Fundamentals, Fabrication and Applications* ed H Weinstock (Dordrecht: Kluwer) pp 117–8
Weinstock H (ed) 1996 *SQUID Sensors: Fundamentals, Fabrication and Applications* (Dordrecht: Kluwer)
Wikswo J P Jr 1989 Biomagnetic sources and their models *Advances in Biomagnetism* ed S J Williamson, M Hoke,

G Stroink and M Kotani (New York: Plenum) pp 1–18

——1995 SQUID magnetometers for biomagnetism and nondestructive testing: important questions and initial answers *IEEE Trans. Appl. Supercond.* **5** 74–120

Williamson S J and Kaufman L 1990 Theory of neuroelectric and neuromagnetic fields *Auditory Evoked Magnetic Fields and Electric Potentials (Adv. Audiol.)* ed F Grandori, M Hoke and G L Romani (Basel: Karger) pp 1–39

Yoshimoto T, Kotani M, Kuriki S, Karibe H and Nakasato N (eds) 1999 *Recent Advances in Biomagnetism* (Sendai: Tohoku University Press)

Zimmerman J E and Silver A H 1966 Macroscopic quantum interference effects through superconducting point contacts *Phys. Rev.* **141** 367–75